

Alma Mater Studiorum – Università di Bologna

DOTTORATO DI RICERCA IN

Disegno e Metodi dell'Ingegneria Industriale e
Scienze Aerospaziali

Ciclo XXIV

Settore Concorsuale di afferenza: 09/A1 Ingegneria Aeronautica,
Aerospaziale e Navale

Settore Scientifico disciplinare: ING-IND/05 Impianti e Sistemi Aerospaziali

TITOLO TESI

**INVESTIGATION ON THE NAVIGATION ANOMALY OF
PIONEER 10 AND 11 PROBES**

Presentata da: Ing. Dario Modenini

Coordinatore Dottorato

Prof. Vincenzo Parenti Castelli

Relatore

Prof. Paolo Tortora

Esame finale anno 2012

Summary

The present work consists of the investigation of the navigation of Pioneer 10 and 11 probes becoming known as the “Pioneer Anomaly”: the trajectories followed by the spacecrafts didn’t match the ones retrieved with standard navigation software. Mismatching appeared as a linear drift in the Doppler data received by the spacecrafts, which has been ascribed to an approximately constant sunward acceleration of about $8.5 \times 10^{-10} \text{ m/s}^2$. The study presented hereafter tries to find a convincing explanation to this discrepancy.

The study is performed based on the analysis of Doppler tracking data through the ODP (*Orbit Determination Program*), developed by NASA/JPL. The research followed a sort of trial/error approach which can be summarized as follows: seek for any kind of physics affecting the dynamics of the spacecraft or the propagation of radiometric data, which may have not been properly taken into account previously, and check whether or not these might rule out the anomaly. In this respect, a major effort has been put to build a thermal model of the spacecrafts in order to predict the recoil force due to anisotropic thermal radiation, since this non-gravitational force is not natively included in the ODP.

Tracking data encompassing more than twenty years of Pioneer 10 interplanetary cruise, plus twelve years of Pioneer 11 have been analyzed. The processing of the data has been carried out in light of the results of the thermal model. Different strategies of orbit determination have been implemented, encompassing single arc, multi arc and stochastic filters, and their performance compared. Orbital solutions have been obtained *without* the needing of any acceleration other than the thermal recoil one indicating that this is most likely the only responsible for the observed linear drift in the Doppler data. As a further support to this we checked that inclusion of additional constant acceleration as does not improve the quality of orbital solutions. All the tests performed lead to the conclusion that no anomalous acceleration is acting on Pioneers spacecrafts.

Sommario

La tesi presenta i risultati e i metodi di uno studio su un'anomalia nella navigazione delle sonde Pioneer 10 e 11, divenuta nota negli ultimi quindici anni come la "Pioneer Anomaly". Le traiettorie seguite da queste sonde non sono esattamente corrispondenti a quelle calcolate a partire dai dati radiometrici ricevuti a terra attraverso il software di navigazione in uso. L'anomalia si è palesata nella pratica come una deriva lineare nei residui dei dati Doppler ricevuti dalle sonde, che è stata attribuita ad una accelerazione eliocentrica approssimativamente costante eliocentrica pari a circa $8.5 \times 10^{-10} \text{ m/s}^2$. Lo studio qui presentato si è posto l'obiettivo di trovare una spiegazione convincente al fenomeno. La ricerca è stata portata avanti basandosi sull'analisi dei dati Doppler tramite il programma ODP (Orbit Determination Program) sviluppato dal Jet Propulsion Laboratory (JPL). L'approccio seguito è stato quello di prendere in considerazione diversi effetti fisici che, influenzando la dinamica della sonda o più in generale la modellazione delle osservabili radiometriche, potessero aver dato origine ad un'apparente anomalia qualora non adeguatamente inclusi nel processo di determinazione orbitale (in altre parole, errori di modello). Tra i vari effetti considerati, il più significativo si è rivelato essere la spinta dovuta alla radiazione termica anisotropa, per la cui stima si è sviluppato un modello termico della sonda.

I dati Doppler analizzati coprono oltre vent'anni di crociera interplanetaria di Pioneer 10, e dodici anni per Pioneer 11. Il processo di determinazione orbitale è stato aggiornato in modo da includere l'effetto della spinta da radiazione termica precedentemente calcolato. Sono state prese in considerazione diverse implementazioni del filtro di stima interno ad ODP, singolo arco, multi arco e filtro stocastico, confrontandone le prestazioni. In particolare, si sono ottenute soluzioni orbitali soddisfacenti *senza* dover ricorrere all'introduzione di ulteriori accelerazioni oltre a quella di origine termica, indicando che. Ulteriore supporto a ciò si ha avuto dalla verifica che l'inclusione di un termine aggiuntivo di accelerazione costante non migliora

la qualità dei residui della soluzione. Tutti i risultati ottenuti portano ad escludere l'esistenza di accelerazione anomala agente sulle sonde Pioneer.

Acknowledgments

This report represents my Ph.D. Thesis in Aerospace Engineering at the II School of Engineering of the University of Bologna.

It presents the work I've done in the last three years at the Radio Science and Planetary Exploration Laboratory at Forlì Campus of the Second Faculty of Engineering. In these years I surely received lots of help from the students and the staff, and I found a friendly environment thanks to which this period has been fruitful, but also enjoyable.

First I would like to thank my supervisor: Prof. dr. Paolo Tortora, for the advices and the guidance during this project.

I also have to thank my colleagues at the Lab, for the stimulating discussions which surely helped improving my understanding on the subject.

Above all, special thanks are due to my family and to Camilla, for their support, their love and their encouragements during the university years.

Dario Modenini

Forlì, March 2012

Contents

<i>Summary</i>	<i>II</i>
<i>Sommario</i>	<i>III</i>
<i>Acknowledgments</i>	<i>V</i>
<i>Contents</i>	<i>VI</i>
<i>Nomenclature</i>	<i>X</i>
<i>1</i>	<i>1</i>
<i>Introduction</i>	<i>1</i>
1.1 Outline of the thesis	4
<i>2</i>	<i>5</i>
<i>Pioneer 10-11 probes and their navigation anomalies</i>	<i>5</i>
2.1 Pioneer 10 & 11 missions	5
2.2 Spacecrafts configuration and operational characteristics	7
2.3 The Pioneer Anomaly: literature survey	10
2.3.1 Contributions of this research to the Pioneer Anomaly Investigation.	13
<i>3</i>	<i>15</i>
<i>The thermal model of Pioneer spacecraft</i>	<i>15</i>
3.1 Why building a thermal model of Pioneer spacecrafts?	15
3.2 Background of radiation theory	17
3.3 Radiation pressure	22
3.4 Energy Balance	23
3.5 Solar radiation pressure	24

3.6	Geometric model and numerical implementation	24
3.7	Simulations set up and convergence check.....	28
3.8	Sensitivity analysis	30
3.9	Fitting of Monte Carlo Simulations	31
4	41
	<i>Orbit analysis of radiometric data</i>	<i>41</i>
4.1	Spacecraft navigation and orbit determination via the ODP	41
4.1.1	Dynamical models.....	42
4.1.2	Observable generations	44
4.1.3	Parameters estimation	45
4.2	ODP subroutines	47
4.3	Criteria for estimate check.....	50
4.4	The tracking data.....	52
4.5	Filtering techniques for orbit analysis	54
4.5.1	Single-arc analysis	54
4.5.2	Multi-arc analysis.....	55
4.6	Data preparation and editing.....	58
5	59
	<i>Results.....</i>	<i>59</i>
5.1	Analysis on first set of data prior to thermal modeling.....	59
5.1.1	Comparison with other published solutions	63
5.2	Orbit analysis of Pioneer 10 and 11 complete set of data in light of thermal model.	68
6	81
	<i>Conclusions and recommendations.....</i>	<i>81</i>
6.1	Conclusions.....	81
6.2	Recommendations.....	82
A	83

<i>Estimation Filters within the ODP</i>	83
6.3 Square-root implementation	85
7.....	88
<i>References</i>	88

Figures Index

Figure 1: Pioneer 10 prototype hanged in the Smithsonian National Air and Space Museum.	4
Figure 2: Pioneer 10 and 11 trajectories projected on ecliptic plane (source: nasa.gov) .	7
Figure 3: Pioneers 10&11 geometric configuration from [PC-202].....	8
Figure 4: Heat dissipated by louvers blade assemblies (left) and louvers structure (right) from design documentation.	26
Figure 5: Louvers arrangement on bus, taken from (TRW Systems, 1971).....	27
Figure 6: geometry model (left) and sample plot of emitted radiation from Pioneers thermal analysis.	29
Figure 7: irradiation reflected by HGA back-side taken from a sample thermal simulation. Contribution from RTG’s heat on two edge regions is evident.	29
Figure 8: radiosity emitted by the back side of the compartment bus, taken from a sample thermal simulation. Contributions from heat rejected by louver is indicated by the red annular region.	30
Figure 9: Pioneer 10&11 RTG’s power measured prior to launch, taken from (Slava G. Turyshev & Toth, 2008)	35
Figure 10: Pioneer 10 RTG’s thermal power (red curve) and electrical power dissipated inside S/C bus retrieved from telemetry, taken from (Slava G. Turyshev & Toth, 2008).	36
Figure 11: Acceleration due to emitted radiation by Pioneer10 (full line) and Pioneer 11 (dash-dot line) along the part of trajectories covered by analyzed tracking data. Spot in Pioneer 11 corresponds to Saturn fly-by.....	39
Figure 12: Schematics of the process of orbit determination.	47
Figure 13: Schematics of the orbit determination process through ODP subroutines....	50

Figure 14: Schematics of the implementation of multi arc data analysis within ODP...	58
Figure 15. Doppler residuals (Hz) in proximity of June 1 st 1987 maneuver.	60

Tables Index

Table 1: Thermo-optical properties of main Pioneers' surfaces.	25
Table 2: Estimated coefficients and formal covariance of the linear regression of thermal recoil force w.r.t input power sources.	33
Table 3: Fitting coefficients and covariance of Pioneer 10 thermal recoil force as a function of time.....	37
Table 4: Uplink and down link frequencies of DSN.	52
Table 5: Summary of preliminary analysis of Pioneer 10 first set of radiometric data (1987-98).	67
Table 6: Parameters treated as consider with relative covariance (nomenclature follows ODP syntax, see footnote for explanations).	68
Table 7: Summary of Test Set 0 of orbit analyses of Pioneer 10 and 11 with estimation of anomalous acceleration.	72
Table 8: Summary of Test Set 1 of orbit analyses of Pioneer 10 and 11 with thermal recoil acceleration included as dynamical model.	75
Table 9: Summary of Test Set 2 of orbit analyses of Pioneer 10 and 11 with thermal recoil acceleration included plus additional acceleration as solve for.....	78

Nomenclature

Latin

<i>A</i>	area	$[m^2]$
<i>a</i>	acceleration	$[m/s^2]$
<i>C_p</i>	specific heat at constant pressure	$[J/(kg\ K)]$
<i>c</i>	speed of light	$[m/s]$
<i>e</i>	spectral radiance	$[W/(m^2\ \mu m)]$
<i>E</i>	power density	$[W/(m^2)]$
<i>H</i>	irradiance	$[W/(m^2)]$
<i>h</i>	Planck's constant,	$[J\ s]$
<i>I</i>	radiation intensity	$[W/(m^2)]$
<i>J</i>	radiosity	$[W/(m^2)]$
<i>k</i>	conductivity, Boltzmann's constant	$[W/(m^2\ K)], [J/K]$
<i>l</i>	optical path	$[m]$
<i>q</i>	heat flux	$[W/(m^2)]$
<i>t</i>	time	$[s]$
<i>T</i>	temperature	$[K]$

Greek

α	absorption coefficient	[-]
ε	emissivity	[-]
Γ	covariance matrix	[-]
λ	wavelength	[-]
ν	frequency	[Hz]
ρ	reflectivity coefficient	[-]
σ	Stefan-Boltzmann constant, standard deviation	[W/(m ² K ⁴)]
τ	transmissivity coefficient, seconds past epoch	[-], [s]

Abbreviations

BOL	Beginning Of Life
EOL	End Of Life
HGA	High Gain Antenna
MLI	Multi Layer Insulation
RHU	Radioisotope Heater Units
RTG	Radioisotope Thermal Generators
SOS	Sum of Squares
WLSQ	Weighted Least Square
w.r.t.	with respect to
OD	Orbit Determination
ODP	Orbit Determination Program
SRP	Solar Radiation Pressure
TCA	Thruster Cluster Assemblies
TRF	Thermal Recoil Acceleration
TRA	Thermal Recoil Acceleration

Introduction

Nearly 40 years ago, on 2nd March 1972, Pioneer 10 was launched from Cape Canaveral, being the first probe directed towards one of the outer planets of the Solar System. Pioneer 10 launch was followed in the 5th of April of the following year, by the one of Pioneer 11. Thanks to gravity assists around Jupiter, and, for Pioneer 11, around Saturn, the two spacecrafts inserted into heliocentric hyperbolic orbits such that on 10th October 1984 Pioneer 10 became the first human artifact to leave the Solar System.

As such Pioneer 10 and 11 allowed for the first time to put the gravity law under test at large heliocentric distances: being highly precisely navigated thanks to their spin stabilizations, the two probes were sensible to accelerations as low as of 10^{-10} m/s². However, quite surprisingly, the radiometric data sent by the probes fell slightly apart from Newton's inverse square law in the outer regions of the Solar System.

This discrepancy, published in 1998 by Anderson et al. (John D Anderson et al., 1998) has been named since then as the "*Pioneer Anomaly*": it practically appears as a linear drift in the difference (residuals) between the Doppler signals received by the probes and the ones computed from the trajectories reconstructed using the state of the art tools for spacecraft dynamics. In particular, the difference between observed and computed Doppler signals has been interpreted as a constant sunward acceleration, pulling back the probes in their journey outside the Solar System. The magnitude of the acceleration as reported in 2002 by Anderson et al. (J. Anderson, Laing, et al., 2002) is $(8.74 \pm 1.73) 10^{-10}$ km/s²; this value is the result of a joint analysis of tracking data through NASA/JPL's Orbit Determination Program (ODP) and a comprehensive error budget taking into account the possible source of errors (dynamics, environmental,

propagation, computational). The conclusion was that no systematic could rule out the anomaly.

Since its discovery, the anomalous acceleration have been independently confirmed by other authors such as Markwardt (Markwardt, 2002), Levy et al. (Levy et al., 2009), and lots of attempts have been made to find a plausible explanation to the origin of the discrepancy; however, no conventional effects have been found to be completely satisfactory, leading some authors to suggest more unconventional causes. These include modifications of the gravity law at scales of the Solar System size, or even the presence of “dark matter”, see for example Jaekel and Reynaud (S Reynaud & Jaekel, 2008) or Brownstein and Moffat (Brownstein & Moffat, 2006). Such theoretical frameworks, however, should be consider with caution and after having excluded with enough confidence any possible modeling error in the reconstruction of the trajectory and of the signal propagation.

Anyhow, the growing interest of the scientific community towards what can be regarded as the only experimental evidence contradicting the gravity law as presently known, motivates this research activity, aimed at finding engineering explanations to the anomaly.

Among the systematic effects, the recoil force originated by anisotropically emitted thermal radiation is one of the most promising to account for, at least partially, the anomaly. Even if in their early investigations Anderson et al. discarded the thermal recoil force (TRF) as a source of a significant bias acceleration, its study has been the subject of recent works, e.g. (Bertolami, Francisco, Gil, & Páramos, 2008), (Bertolami, Francisco, Gil, & Páramos, 2010). (L & Rievers, 2009; Rievers, Bremer, List, Lämmerzahl, & Dittus, 2010). It is indeed clear that, having the craft only one plane of symmetry, its emitted thermal radiation is likely to be quite anisotropic, justifying an in-depth analysis of the matter. On top of that, new interest in TRF evaluation arose thanks to the telemetry data recently recovered at JPL, (Slava G. Turyshev & Toth, 2009), which includes measurements of the thermal state of the probes, providing a valuable support for such analysis.

The research activity presented herein has been totally carried out at the Radio Science and Planetary Exploration lab of the Second School of Engineering, and is articulated in two main parts:

Pioneer 10 & 11 probes

1. development of a thermal model of Pioneer 10 probe along its interplanetary cruise, with particular focus on the integration in the orbital analysis.
2. Analysis of radiometric Doppler data of Pioneer 10 ranging from 1979 to 2002, and for Pioneer 11 in the period 1977-1979 and 1980-1990. The analysis has been performed with the ODP (Orbit Determination Program) software.

1.1 Outline of the thesis

The thesis is organized as follows. Chapter 2 summarizes Pioneers 10 & 11 missions and spacecrafts' characteristics, and includes a survey of the literature on the Pioneer Anomaly. In chapter 3 the thermal model of the spacecraft will be presented. Chapter 4 deals with the theory of Orbit Determination and its implementation using JPL's ODP (Orbit Determination Program) during this thesis. In chapter 5 the results of the analysis of radio metric data of Pioneer 10 and 11 are presented and discussed. Finally in chapter 6 conclusions drawn from the investigations are presented.

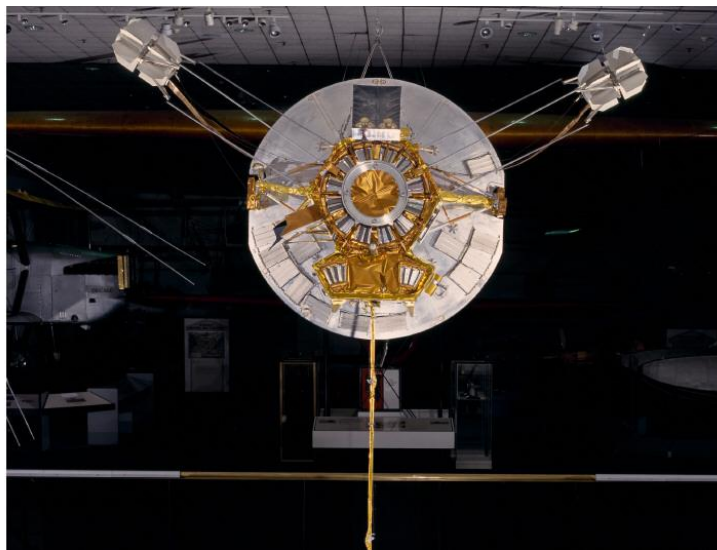


Figure 1: Pioneer 10 prototype hanging in the Smithsonian National Air and Space Museum.

Pioneer 10-11 probes and their navigation anomalies

In this chapter first a brief description of Pioneer 10 and 11 missions and spacecraft configurations will be given focusing on the aspects relevant for the subsequent analysis of the navigation and thermal modeling. Then a literature survey on the subject will be presented.

2.1 Pioneer 10 & 11 missions

Launched on 2 March 1972, Pioneer 10 was the first spacecraft to make direct observations of Jupiter and to travel into deep space. The mission objectives of Pioneer 10, and of its sister probe Pioneer 11, can be summarized as:

- Explore the interplanetary medium beyond the orbit of Mars;
- Investigate the nature of the asteroid belt and assess its hazard to future missions.
- Explore the environment of Jupiter and Saturn, in particular their radiation belts and magnetic fields.
- Explore solar atmosphere, heliosphere, and cosmic rays transport into it.

During its Earth-Jupiter cruise two correction maneuvers, on March 7th and 24th, were performed to correct its trajectory towards Jupiter at the desired encounter distance.

By January 1973 Pioneer 10, more than 3 AU beyond the asteroid belt, entered Jupiter gravitational sphere of influence. During its Jupiter encounter (closest approach at 2.8 Jupiter radii), Pioneer 10 imaged the planet and its moons, and took

Pioneer 10 & 11 probes

measurements of Jupiter's magnetosphere, radiation belts, magnetic field, atmosphere, and interior. Thanks to this encounter, Pioneer 10 was boosted on a heliocentric hyperbolic orbit with infinite velocity of 11.3 km/s, sufficient for escaping the Solar System. Pioneer 10 was then able to explore the outer regions of the Solar System, studying solar wind and cosmic rays. The spacecraft continued to make valuable scientific investigations in the outer regions of the Solar System until its science mission ended on March 31, 1997. Doppler data were actually received until 2002, when onboard power dropped below the minimum level required for maintain radio link. Pioneer 10 is now headed in the general direction opposite as the Sun moves in our Galaxy.

Launched on 5 April 1973, Pioneer 11 followed its sister ship to Jupiter (2 December 1974). During its flyby, with closest approach at 1.8 Jupiter radii, the craft was able to gather the first observations of the polar regions. It also measured quite accurately the mass of Jupiter's moon Callisto. After gaining momentum from the Jupiter flyby, Pioneer 11 arrived at Saturn five years later making the first direct observations of the planet including pictures of its rings, and magnetosphere and magnetic field measurements; by that time Voyager 1 and Voyager 2 had already passed Jupiter and were also en route to Saturn. Later Pioneer 11 encountered Saturn's moons Janus and Mimas on September 1, 1979.

After leaving Saturn, Pioneer 11 was placed on a trajectory that would send it flying out of the Solar System. The motion of Pioneer 11 is approximately in the direction towards the heliopause, being roughly opposite to the direction of Pioneer 10 (see Figure 2). The Pioneer 11 mission ended in November 1995, when the last transmission from the spacecraft was received.

The discovery of Pioneer Anomaly can be regarded as a collateral effect of the missions, in the sense that a gravity test was not among the intended objectives.

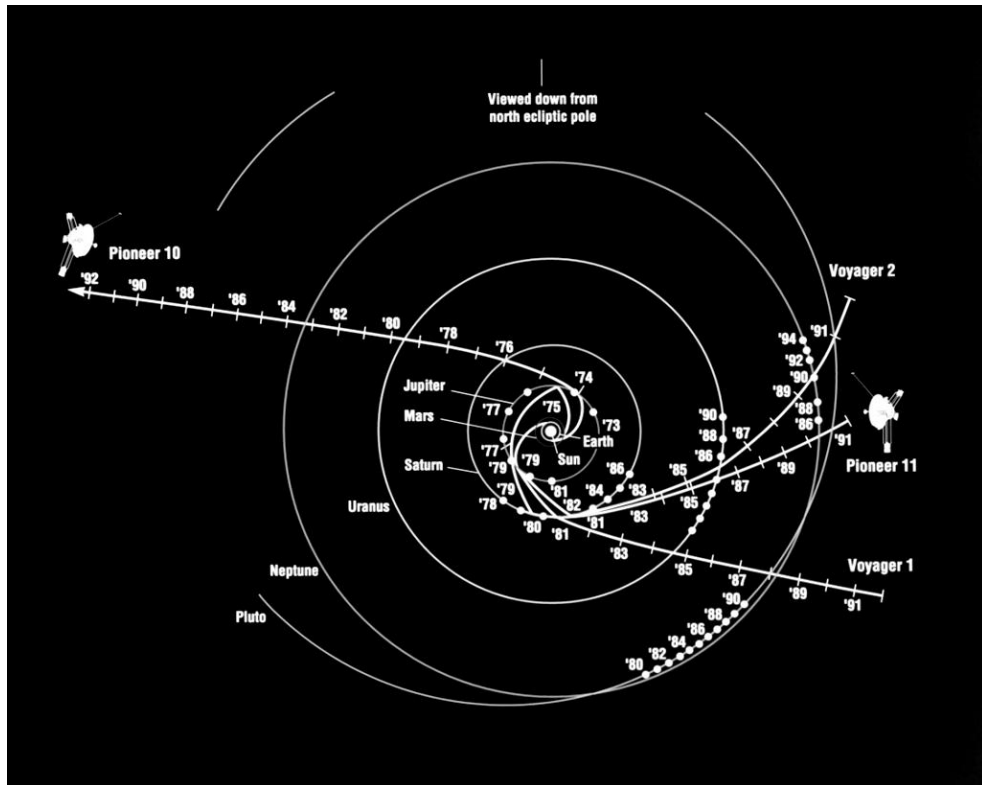


Figure 2: Pioneer 10 and 11 trajectories projected on ecliptic plane (source: nasa.gov)

2.2 Spacecrafts configuration and operational characteristics

Pioneer 10 and 11 are virtually identical; their geometry (see Figure 3) is dominated by three main components: the big parabolic antenna, HGA (High Gain Antenna) of 2.74 m of diameter, the spacecraft body and the radioisotope thermoelectric generators (RTGs). Behind the HGA two compartments are found, a regular hexagonal box, the main compartment, including some electronics and the fuel tank, plus a smaller irregular hexagonal box containing the science instruments. Together the two compartments constitute the spacecraft body. Some other instrumentation was located externally to the S/C body, such as the Plasma Analyzer, the Asteroid/Meteoroid Detector and the Cosmic Ray Telescope.

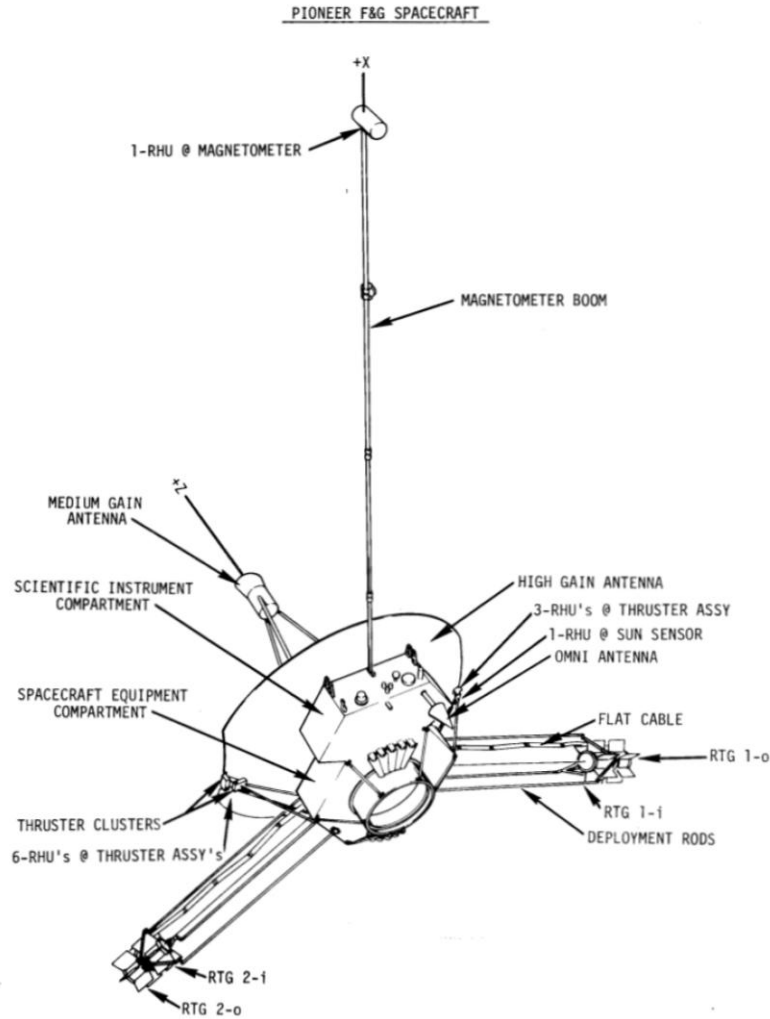


Figure 3: Pioneers 10&11 geometric configuration from [PC-202].

Other major components of the spacecrafts are two couples of radioisotope thermoelectric generators (RTG), attached to the body through 3m long booms separated at an angle of 120° . Separation of RTGs from spacecraft body is required to minimize both thermal and nuclear radiation exchange. In pre-launch configuration the booms were folded towards the equipment compartment; deployment was initiated soon after launch thanks to pyrotechnic actuators and sustained by the centrifugal force imparted by the spin motion. A third boom, visible in Figure 3, is present holding the magnetometer. The RTGs represent the power source of the spacecraft and are fueled by ^{238}Pu isotope. The BOL thermal output was around 2580W, turned into 160 W of electrical power thanks to thermopiles. Excess power¹ available at early stages of

¹ Nominal power consumption was $\approx 100\text{W}$.

mission was stored into an 8-cells Ag-Cd battery or dissipated into space as thermal energy thanks to a shunt resistor radiator. It's important to underline (the reason will be clarified later in the report) that the electrical power, as well as the thermal power, output decreases over time as a result of degradation of thermopiles efficiency and plutonium decay. As a consequence, during the extended mission the available electric power dropped below 100 W being sufficient for HGA pointing, operating transmitter and receiver and for command and data handling, while all scientific instrumentation was kept off.

The two spacecrafts were equipped of a monopropellant propulsion system fueled by hydrazine. Thanks to a catalyst, the propellant dissociates into hot gas and expands through the thruster nozzles. In particular six thrusters capable of 11lb of thrust each, grouped in three Thruster Cluster Assemblies (TCA), were placed on the HGA perimeter. The system was aimed at three types of maneuvers: precession maneuvers, that is, re-pointing of HGA towards the Earth to ensure communication link, delta-V maneuvers for trajectory control, and spin/de-spin maneuvers.

Both spacecrafts were spin stabilized, spin axis being the axis of the HGA, with a nominal velocity of 4.8 rpm for P10 and 7.8 rpm for P11. The mass at launch was nearly 259 Kg, a value which slowly decreased during the many years of operation life due to fuel consumption.

Thermal control is ensured by insulation of the equipment compartment plus a passively controlled heat rejection system. Insulation is provided by aluminized Kapton MLI (Multi-Layer Insulation) covering the structural honeycomb panels. Heat rejection is provided by a louver system consisting of a radiating platform covered by 30 individually actuated blades grouped in two 3-blades assemblies on the aft side of the experiment platform, and twelve 2-blades assemblies mounted radially around the separation ring. The angular position of the blades is altered by a set of bimetallic springs whose actuation range lies between 85F (fully closed configuration) and 40F (fully open configuration).

Uplink and downlink between the spacecrafts and the DSN stations on Earth is ensured by a communication subsystem at S-band frequencies ($\nu \approx 2.2\text{GHz}$). It may operate both in *one-way* and *two-way* Doppler measurement mode: the former consists in the transmission to a DSS of a non-coherent radio signal when no uplink signal is present. The latter consists in the phase coherent retransmission of an uplink signal,

originally at 2.29 GHz, with a transponding ratio of 240/221. Actually, since at large geocentric distances the round-trip light time (RTLTL) gets beyond 8 hrs, the transmitting and receiving stations must be different, giving rise to a *three-way* measurement. Besides Doppler measurement, the communication subsystem also receives and demodulates commands sent by DSS, transmits data gathered by the scientific instrumentation and engineering data from various sensors placed onboard, and implements the conical scanning of HGA which generates a signal (*conscan*) to be supplied to the Attitude Control Subsystem to control timing of precession maneuvers. In addition to the HGA, which was used at long ranges, a medium gain/omni-directional antenna is also present, which provided broad-angle communications at short ranges.

2.3 The Pioneer Anomaly: literature survey

There is a huge amount of literature regarding the Pioneer Anomaly since the last 15 years: in this section a roadmap of the relevant sources will be briefly presented. Before going into this, we mention the source which constitutes a prerequisite before facing the topics of orbit determination and navigation: the “Bible” of the subject written by T. D. Moyer at JPL, in two parts: (Moyer, 1971) and (Moyer, 2000). These references are dedicated to the specific implementation of the ODP but represent at the same time an impressive compendium of the theoretical and practical aspects of the orbit determination in general.

The first paper on the Pioneer Anomaly is dated 1998 (John D Anderson et al., 1998), it reports the estimated value of constant anomalous acceleration and investigates some possible explanations: errors in modeling of non-gravitational forces, modification of gravity law or presence of dark-matter. In this paper heat reflected by HGA is already mentioned as possible explanations but disregarded as not contributing for a substantial bias acceleration. In the later work of 2002, a comprehensive investigation is performed which accounts for all possible systematic. This has been for years the most complete survey on the subject, including almost all the important aspects of data analysis and orbit determination algorithms. Orbit analyses are reported being performed using JPL’s ODP and Aerospace Corporation’s CHASMP (*Compact High Accuracy Satellite Motion Program*) software on a batch of Pioneer 10 data from 1987 to 1998 and Pioneer 11 data from 1987 to 1990. A comprehensive error budget was performed taking into account on board systematics, effects due to sources external to the spacecraft and

computational errors. The conclusion was that none of these sources could rule out the drift found in Pioneers post-fit residuals. The result of the error budget was combined with the orbital solutions obtained to get to a “global” result for the Pioneer Anomaly (which can be regarded as the benchmark for the present study) of $a_P = (8.74 \pm 1.33) \times 10^{-10} \text{ m/s}^2$. Superimposed to the constant acceleration, they also found an oscillatory term of annual period and amplitude of about $1.6 \times 10^{-10} \text{ m/s}^2$, for which they suggested a likely cause to be incorrect modeling in orbital inclination of the spacecraft to the ecliptic plane.

The presence of the anomaly has been independently confirmed by other authors using different software for spacecraft navigation; besides the ODP, we mention:

1. CHASMP code from Aerospace Corporation (J.D. Anderson, Laing, et al., 2002; John D Anderson et al., 1998);
2. Code written by C. B. Markwardt (Markwardt, 2002);
3. Orbit determination code by V. T. Toth (V.T. Toth, 2009);
4. ODISSEY developed by Levy et al. (Levy et al., 2009) specifically to study the Pioneer Anomaly.

All these independent studies were able to confirm the presence of the anomalous acceleration with similar magnitudes. Moreover in their works Toth and Markwardt were able to confirm that the tracking data are compatible with a moderate jerk term (jerk = time derivative of acceleration). The jerk terms were reported to be for Pioneer 10, $(-0.18 \pm 0.12) \times 10^{-10} \text{ m/s}^2$ (Markwardt) and $(-0.21 \pm 0.04) \times 10^{-10}$ (Toth); for Pioneer 11 a value of $(-0.34 \pm 0.12) \times 10^{-10} \text{ m/s}^2$ is given by Toth.

Levy et al. performed a spectral analysis of the best-fit residuals after the application of a constant bias acceleration which highlighted peaks with terms of half a day, one day and six months. They investigate the effect of adding a periodic Doppler shift to the data, function of the Sun-Earth-Probe angle, which resulted in a sensible decrease of residuals standard deviation.

A number of mechanisms have been considered also by Nieto and Anderson as attempts of explanations of the anomaly as a systematic effect generated by the spacecraft itself or its environment (Michael Martin Nieto, Anderson, & Alamos, n.d.).

Because of failing to find conventional explanations to the anomalous acceleration, some theories regarding possible new physics began to rise. These unconventional

explanations are not of much interest for the present work, and just an incomplete list of them is given hereafter² divided into two main groups:

- Modified gravity theories; which include scale dependent modifications to gravity potential, Modified Newtonian Dynamics; dark matter or dark energy, scalar tensor fields of gravity.
- Cosmological motivations, such as the effects of the expanding universe on planetary orbits, radio signal propagation, clock acceleration.

In 2003 Scheffer (Scheffer, 2003) put forward the anisotropic thermal radiation as the main cause for the anomalous acceleration, without the needing of new physics. Since then, several other authors devoted their efforts to estimate the thermal dissipation force, see e.g. (Bertolami & Páramos, 2007), (Bertolami et al., 2010), (L & Rievers, 2009), (Rievers et al., 2010). An interesting contribution to this subject came from Toth and Turyshev (V. Toth & Turyshev, 2009) which provided a rigorous theoretical frame for the computation of the force acting on a body due to the emitted thermal radiation.

Rievers et al. developed a ray tracing algorithm with which they estimated the amount of RTG's heat reflected from the back of the HGA contributing as much as one third of the anomalous acceleration. The earlier work of Bertolami et al. (Bertolami et al., 2010) reported that a fraction of the anomaly between 35 to 57 % of the anomalous acceleration could be explained by the thermal dissipation force. However, their updated model, based on Phong shading technique, reports that the acceleration arising from thermal radiation has a similar order of magnitude to the constant anomalous acceleration, claiming that the Pioneer Anomaly can be finally put to rest (Francisco & Bertolami, 2011).

Recently an impressive survey of the Pioneer Anomaly investigation has been published by Turyshev and Toth (Slava G. Turyshev & Toth, 2008) which constitutes the most complete reference of the subject including reviews of all the efforts performed to finally put the anomaly to rest. Temporally varying behavior of the anomaly has also been the object of the most recent paper by Turyshev and Toth (S.G. Turyshev, Toth, Ellis, & Markwardt, 2011), where they conclude that a jerk term of $\approx 2 \times 10^{-10}$ m/s²/year provides a 10% improvement of residuals. In this paper they also faced two other open questions: the onset of the anomaly and its exact direction. Their conclusions are that it

² For an in-depth review of the subject see (Slava G. Turyshev & Toth, 2008)

is not possible to precisely discern the between Sun-pointing, Earth pointing or spin axis directions for the acceleration, and that pre-Saturn encounter Pioneer 11 data cannot support for an early onset of the acceleration.

2.3.1 Contributions of this research to the Pioneer Anomaly Investigation.

Due to the large number of efforts devoted to the cause of solving the Pioneer Anomaly, it is reasonable to ask which is the contribution brought by the present research.

From the discussion presented in section 2.3, it emerges that the most promising candidate to explain the anomaly seems to be the thermal dissipation force. Because of this the efforts of several authors in the last years were devoted to one of the two aspects below:

- 1- build a thermal model of the spacecrafts to estimate the thermal recoil force, and compare it with published results for the anomalous acceleration
- 2- check for the compatibility of the tracking data with a jerk term with a time constant compatible with the radioactive decay of Plutonium

The present work combines in a sense these two approaches: a thermal model have been developed oriented to its successive integration in the orbit determination process such to verify *a-posteriori* the compatibility of the tracking data with the thermal dissipation force. The level of detail of the model is in some way intermediate with respect to the ones found the cited references: it relies on a FEM software which solves the conduction-radiation heat equations on a simplified probe geometry, and allows for a sensitivity analysis of the solution to the uncertain parameters. This choice has been guided by the feeling that, even if a highly detailed geometric model of the spacecraft could in principle have been built based on available design documentation and telemetry temperature data, its accuracy would have an intrinsic limit anyway since after many years of interplanetary cruise the properties of materials and temperature sensors performance may have considerably degraded. Therefore, the accuracy achievable by a highly detailed model of the spacecraft would have an intrinsic limit anyhow.

On the orbit determination side, a contribution to the investigations performed is given by the inclusion of deterministic dynamic compensation *via* a multi-arc filter which is a capability included in the ODP. Stress has been also put to properly model

Pioneer 10 & 11 probes

the more than one hundred precession maneuvers which were performed by Pioneers in the period covered by the data, since it has been verified that they considerably affect the quality of post-fit residuals.

Globally, this research has the objective of put the word end to the 15 years long lasting Pioneers puzzle.

The thermal model of Pioneer spacecraft

This chapter deals with the engineering model which has been set up for estimating the force acting on a spacecraft due to anisotropic thermal emission. First the reasons which motivates the effort of building a thermal model of the spacecrafts are discussed. Then, a brief discussion of the physics underlying the phenomenon, i.e. radiative heat transfer and radiation pressure, will be presented. Then a more in depth analysis will be given concerning the thermal model of the Pioneer spacecrafts and the strategy used to integrate the output of such model in the process of orbit determination.

3.1 Why building a thermal model of Pioneer spacecrafts?

As stated in section 2.2 the main sources of power on board Pioneer spacecrafts are four radioisotope thermoelectric generators (RTGs) which generated nearly 2580 W at launch. This power decays during the mission following plutonium 87.7 years half-life time. A fraction of this thermal power (≈ 160 W at launch) is converted into electrical power: part of this power is transmitted towards the Earth as a radio beam, while the remaining part is consumed by the instrumentation placed inside and outside the spacecraft body to be eventually converted into heat. The waste heat is radiated into space through the main compartment MLI blankets and a louver system which ensures thermal control of the spacecraft. In other words, all power input to Pioneers spacecrafts is expelled in form of electromagnetic radiation (either IR or electromagnetic), which carries momentum with it. If the radiation pattern is anisotropic, momentum exchange between the spacecraft and the radiation results in a dissipation force which affects the

trajectory of the probe. In particular the component of radiation force on a certain direction equals the unbalanced power output in the same direction divided by the speed of light. Therefore a simple order of magnitude analysis tells us that, the mass of the spacecrafts being about 250 Kg, only 63 W, which are a very small fraction of the total available power, if directionally radiated away from the sun would cause an acceleration equal to the anomaly. It is hence clear that the recoil force due to radiation should be properly estimated and if relevant, included in the orbit determination process.

By inspection of the macroscopic configuration of Pioneer geometry as visible in Figure 1 and Figure 3 one can identify at least two mechanisms which are likely to be responsible of a certain degree of anisotropy in radiation emission:

- 1- Heat from RTGs reflected back by the highly reflective backside of the HGA;
- 2- Electrical heat dissipated inside the bus having a preferred escape direction through the louver system.

Both this contributions are directed as the anomaly (that is HGA axis). We note here that first contribution depends on thermal power, while second on electrical power. There is actually another source of thermal energy onboard other than the RTG's which are 9 radioisotopes heaters units (RHU) generating 1W each, and deputed to heat up thruster cluster assemblies. However, according to Turyshev (Slava G. Turyshev & Toth, 2008) their geometric configuration and location is such to prevent them to contribute substantially to anisotropic radiation.

In various papers (J.D. Anderson, Laing, et al., 2002) it has been pointed out that the secular time evolution of RTG's power is quite in contrast with the evidence of a constant anomaly, even if Markwardt (Craig B. Markwardt, 2002) and Toth ((V.T. Toth, 2009)) claimed that the Doppler shift is compatible with a jerk term of a time scale similar to the decay of Plutonium. More recently, Turyshev (S.G. Turyshev et al., 2011) arrived to a similar conclusion using extended data sets of both Pioneer 10 and 11. These arguments assume that the thermal dissipation force, being proportional to the power generated on board, should exhibit a monotone time decrease. However, infrared emission from the spacecraft's surfaces is proportional to the total energy input to the spacecraft, which, besides RTG's power, also includes irradiation from the Sun. Solar flux effect on spacecraft dynamics is twofold: on one side there is the solar radiation pressure, which is commonly accounted for during trajectory integration (ODP implements a model to estimate momentum exchange between solar flux and spacecraft

components, see section 4.1.1). On top of that, solar flux induces a temperature rise on the surfaces on which it impinges on, due to the fraction of radiation which is adsorbed. For the Pioneers, this is the case especially for the high gain antenna which is constantly pointed towards Earth and also fully illuminated by the Sun, at least at sufficiently large heliocentric distances. The parabolic dish is basically a thin surface with highly different emittance on the two sides: the backside of the antenna is highly reflective with a low emittance, on contrary, the white painted front-side is highly emissive (see data in Table 1). Therefore almost all of the solar power is dissipated by the side facing the Earth; this results in a recoil force anti-parallel to the contribution coming from internally generated power, hence subtracting to its amount. The subtracting term coming from the solar flux decreases in time because of the probes motion receding from the Sun, such that, as will be shown later, the thermal model developed reconstructs a recoil force which is not decreasing in time monotonically.

3.2 Background of radiation theory

All forms of matter at nonzero absolute temperature emit radiation: for gas and some kind of semitransparent solids emission is a volumetric phenomenon, that is, the overall radiative output from the body is an integrated effect of the local molecular emission throughout the volume. For most solids and liquids emission is, on the other hand, a surface phenomenon because radiation emitted from interior molecules is absorbed by the neighbor molecules. The theory summarized in this paragraph (Modest, 2003) applies to this latter group.

The physical law which correlates the absolute temperature T of a body and the energy radiated in vacuum, is given by Planck's law for monochromatic emissive power:

$$E_{\lambda}(\lambda, T) = \frac{\varepsilon_{\lambda} 2\pi h c_0^2}{\lambda^5 \exp\left[\frac{hc_0}{k_B T \lambda} - 1\right]} = \varepsilon_{\lambda} \times E_{b\lambda}(\lambda, T) \quad (4-1)$$

where ε_{λ} is the *monochromatic emittance*, c_0 is the speed of light in vacuum, 2.997924×10^8 m/s, h is Planck's constant, $6.62606876 \times 10^{-34}$ J·s, k_B is Boltzmann constant, $1.3806503 \times 10^{-23}$ J/K, λ is the wavelength of the radiation being considered, and $E_{b\lambda}$ is the blackbody monochromatic radiation intensity. For *grey bodies* the

emittance is constant all over the wavelengths: if this constant equals 1 we deal with a *blackbody*.

A blackbody is referred to as a perfect absorber and emitter, in the sense that it absorbs all incident radiation, regardless of wavelength and direction, and emits the maximum amount of energy for a prescribed temperature and wavelength.

By integrating Planck's law over the entire spectrum, the *total heat flux* [W/m²] radiated, E , is obtained (Stefan-Boltzmann law):

$$E = \int_0^{\infty} E_{\lambda}(\lambda, T) d\lambda = \varepsilon \sigma T^4 \quad (4-2)$$

where ε is the *total emissivity* of the body and σ is the Stefan-Boltzmann constant, $5.670400 \times 10^{-8} \text{ W/m}^2 \cdot \text{K}^4$. For gray bodies it holds: $0 < \varepsilon < 1$.

For real bodies emittance is not only function of wavelength but also of the observation angle and the temperature, hence, in general:

$$\varepsilon_{\lambda} = \varepsilon_{\lambda}(\theta, \lambda, T) = E_{\lambda}(\theta, \lambda, T) / E_{b\lambda}(\theta, \lambda, T) \quad (4-3)$$

Which shows how the emittance is the ratio between the intensity of the radiation emitted by a surface at the wavelength λ , temperature T and direction θ and the radiation emitted by a blackbody at the same λ and T . The angle θ belongs to a spherical coordinate system (θ, ψ) with the elevation θ lying in $[0, \pi/2]$ while the azimuth ψ lies in $[0, 2\pi]$. From this definition follows the infinitesimal solid angle $d\Omega$ as: $d\Omega = \sin\theta d\theta d\psi$. For engineering calculations it is common to work with directional averages of the spectral emittance, the so called *hemispherical emittance*.

Since the energy flux involved depends on direction, when dealing with radiation exchange between different absorbing/emitting surfaces, it is convenient to define a new quantity, the *radiative intensity* I , as the radiative energy flow per unit solid angle and unit area *normal to the rays*. Again, as for the emissive power, one may distinguish between *spectral* (i.e. wavelength dependent) and *total* (i.e. integrated all over the wavelengths) radiative intensity: in the following we restrict our attention to the latter.

For a flat, diffuse radiator it can be shown that radiation intensity is independent from the direction of the rays and is related to the emitted power as:

$$I = E/\pi = 1/\pi \times \sigma \epsilon T^4 \quad (4-4)$$

From this relation follows that the *directionally* emitted flux I' (energy flow per unit solid angle and unit emitting area) is then simply calculated by multiplying I for the projected area element normal to the rays, $dA_p = dA \cos\theta$:

$$I' dA = I dA_p = I dA \cos\theta \Rightarrow I' = I \cos\theta \quad (4-5)$$

That is, the directionally emitted power scales with the cosine of the elevation angle: this is usually referred to as *Lambert's cosine law*.

Integration of the radiative intensity emitted by a surface over a hemisphere surrounding it leads to the total power emitted by dA :

$$dE = \int_0^{2\pi} \int_0^{\pi/2} I \cos\theta \sin\theta d\theta d\psi = \sigma \epsilon T^4 \quad (4-6)$$

Besides the emitting properties of a surface, it is of interest for our applications the behavior of a body when subjected to incident radiation (usually called *irradiance*, H): if a monochromatic beam of radiation H_λ hits a body, a fraction $\alpha_\lambda H_\lambda$ is absorbed, a fraction $\rho_\lambda H_\lambda$ is reflected, and a fraction $\tau_\lambda H_\lambda$ is transmitted. The dimensionless numbers α_λ , ρ_λ , τ_λ are respectively, the *absorption*, *reflection* and *transmission* coefficients, for which holds:

$$\alpha_\lambda + \rho_\lambda + \tau_\lambda = 1 \quad (4-7)$$

As for emittance, temperature dependency is of concern; moreover, the absorptance may be different for different directions of irradiation while the magnitude of reflection and transmission may depend on both incoming and outgoing directions. However, for certain applications temperature variation may be safely neglected: such simplification will be retained also in the thermal model of Pioneers for all surfaces but one, the louvers (see section 3.6). Direction dependency may be dropped when referring to hemispherical properties: this latest hypothesis is quite restrictive when applied to reflectivity as it is common to distinguish between *diffuse* reflection and *specular* reflection.

The thermal model of Pioneer spacecrafts

By averaging the three coefficients all over the wavelength spectrum one obtains the *total* hemispherical absorptivity, reflectivity and transmissivity, indicated by α , ρ , τ respectively.

Conservation of energy requires that the amount of radiation emitted by the body equals the absorbed one (Kirchoff's Law), that is:

$$\alpha_\lambda = \varepsilon_\lambda \quad (4-8)$$

In the assumption of gray surface the above equality can be extended from spectral coefficients to the total ones:

$$\alpha = \varepsilon \quad (4-9)$$

The hypothesis of grey surface is often made and is a good approximation for most objects, at least in a limited waveband. An example of this assumption falling apart is quite common in spacecraft application: a spacecraft surface has an absorptance of solar radiation (α_s) which is not equal to its infrared emittance, since radiation emitted by spacecraft and by the Sun happens at very different wavelengths.

Among the different radiative properties of the bodies, we can distinguish some peculiar limiting case:

- $\tau = 0$, $\alpha + \rho = 1$ for opaque bodies:
- $\alpha = \varepsilon = 1$, $\rho = 0$ for perfect emitter, absorber (black body)
- $\alpha = \varepsilon = 0$, $\rho = 1$ for perfect radiative insulators.

For the Pioneer spacecrafts, the hypothesis of opaque grey body can be retained for all the surfaces but the multi-layer insulation blankets (MLI) covering the compartment bus. For such a component an "effective" emissivity, ε_{eff} , can be defined, which is very low (MLI are actually designed to retain heat, that is to have low ε_{eff}) and different from the actual emissivity of its outermost layer ε_{out} . Therefore the reflectivity coefficient is not $1 - \varepsilon_{eff}$, which would generate an extremely high amount of reflected radiation, rather $1 - \varepsilon_{out}$.

After these remarks, the radiative energy balance at a point of a grey, opaque, surface, being a diffuse emitter and reflector, can be stated as follows:

$$J = \rho H + E = \rho H + \sigma \epsilon T^4 \quad (4-10)$$

In (4-10) we have denoted with J the surface *radiosity*, i.e. the *total* heat flux leaving the surface due to emission and reflection. This implies that the *net* outward radiative flux at the surface is given by:

$$q_{out} = J - H = (\rho - 1)H + \sigma \epsilon T^4 \quad (4-11)$$

A further arrangement of (4-11) can be done, since for a grey body $(\rho - 1) = \epsilon$:

$$q_{out} = J - H = \epsilon(\sigma T^4 - H) \quad (4-12)$$

We may also reformulate the relationship between radiation intensity and emitted power, by replacing the latter with the radiosity:

$$J = \pi I \quad (4-13)$$

In order to correctly model the net thermal radiation energy leaving one surface, all surfaces with which it can exchange radiation have to be considered. This introduces shadowing and mutual reflections effects depending on the sizes, and relative positions and orientations of the surfaces, adding quite some complexity to the problem. Actually, also the presence of a medium separating the surfaces should be accounted for since it affects the propagation of electromagnetic waves, therefore the radiation exchange. However we will be restricting ourselves to the case of a *non-participating media*, which for the application of Pioneers' deep space cruise seems a very reasonable assumption. The usual way to account for such effects is by introducing the concept of *view factors* between surfaces. View factor is conveniently define firstly between two infinitesimal surfaces, say dA_i and dA_j , as the portion of (diffuse) radiosity J_i leaving dA_i intercepted by dA_j divided by the total radiation leaving dA_i . It can be easily shown from geometric consideration that this can be calculated as:

$$dF_{dA_i-dA_j} = \frac{\cos\theta_i \cos\theta_j}{\pi r^2} dA_j \quad (4-14)$$

where θ_i (θ_j) is the angle between the surface normal \mathbf{n}_i (\mathbf{n}_j) and the line connecting dA_i and dA_j whose length is r . The extension to finite surfaces is found by double integration of the radiosity over the emitting (A_i) and receiving (A_j) surfaces, divided by the total emitted power:

$$F_{A_i-A_j} = \frac{\int_{A_i} \int_{A_j} J_i \frac{\cos\theta_i \cos\theta_j}{\pi r^2} dA_j dA_i}{\int_{A_j} J_i dA_i} \quad (4-15)$$

One may also try to compute the view factor of a surface with respect to itself: in that case $F_{A_i-A_i}$ is different from zero only for *concave* surfaces.

3.3 Radiation pressure

Radiation energy is propagated through photons travelling at the speed of light c and carrying an energy $h\nu$, therefore carrying momentum equal to $h\nu/c$. If photons hit or leave a surface a momentum transfer takes place giving rise to a force. This force can be expressed in terms of a radiation pressure related to the radiation intensity I .

If we consider a beam of radiation emitted by a surface element dA , directed towards a direction $\hat{\mathbf{s}}(\theta, \psi)$, the energy flow leaving dA is $I \cos\theta dA d\Omega$; the flow of momentum escaping from dA in the normal direction therefore equals:

$$\frac{1}{c} I(\hat{\mathbf{s}}) \cos^2\theta d\Omega \quad (4-16)$$

By Newton's second law, total momentum flux normal to the surface must be counteracted by a pressure force $p_{rad}dA$, found by integration over all directions over a hemisphere surrounding the surface (θ ranging from 0 to $\pi/2$):

$$\begin{aligned} p_{rad} &= \frac{1}{c} \int_0^{\pi/2} \int_0^{2\pi} I(\hat{\mathbf{s}}) \cos^2\theta \sin\theta d\theta d\psi = \frac{1}{c} \int_0^{\pi/2} \int_0^{2\pi} \frac{\sigma \epsilon T^4}{\pi} \cos^2\theta \sin\theta d\theta d\psi \\ &= \frac{2}{3c} dE \end{aligned} \quad (4-17)$$

Integration all over the emitting area leads to the recoil force acting on the element itself.

We mentioned only pressure force (which, by definition, acts on a direction normal to the surface) without speaking of a radiation tangential force since *lambertian* radiation pattern is symmetric in tangential directions.

Similarly, a pressure force may be defined for absorbed or reflected radiation. Such effects may be accomplished by generalizing the definition of radiation pressure and force as:

$$p_{rad} = \frac{k}{c} \int_0^{\pm\pi/2} \int_0^{2\pi} I(\hat{\mathbf{s}}) \cos^2\theta \sin\theta d\theta d\psi \quad (4-18)$$

$$\mathbf{F}_{rec} = \int_A p_{rad} \hat{\mathbf{n}} dA \quad (4-19)$$

Where $\hat{\mathbf{n}}$ is the surface normal versor and $\cos(\theta) = \hat{\mathbf{n}} \times \hat{\mathbf{s}}$ (>0 for an emitted I , <0 for an absorbed or reflected I), while $k = -1$ for emission, $k = 1$ for absorption and $k = (1+2/3)$ for diffuse reflection.

From the above discussion, the evaluation of the net force due to thermal radiation requires the evaluation of the radiative intensity departing and arriving at each surface of the body. In the hypothesis of diffuse emitter and reflector, this implies the computation of the radiosity J and irradiation G , previously defined, which in turn requires the computation of the view factors between different surfaces. Having these quantities, one may compute the radiation pressure due to emission, absorption and reflection at each surface and then sum all the contribution to get the net thermal force. An alternative approach has been followed in the present work, which involves the use of a control volume surrounding the spacecraft. This control volume acts as a sort of “passive” blackbody, that is a body at a constant temperature of 0 K and emissivity of 1, such that it absorbs all the incident radiation without emitting or reflecting anything. In this fashion we can consider the spacecraft as a whole system rather than focusing on the radiation pressure at each surface: the *net* radiation escaping out of this system and detected by the control volume is the only contribution to the recoil force since the contribution due of radiation intercepted (absorbed) by spacecraft components cancels out the pressure acting on the surfaces emitting such radiation.

3.4 Energy Balance

Heat transfer via conduction and radiation takes place as a volumetric and a surface phenomenon: conservation of energy requires that volumetric and surface heat sources input to the system (the spacecraft) balance the net radiation emitted by the system itself and detected by the control volume:

$$\iiint_{V_{Pio}} \dot{Q} dV + \iint_{S_{Pio}} \vec{q}_{Sun} \times \vec{n} dS = \iint_{S_{Pio}} (J - H) dS = \iint_{CV} H dS \quad (4-20)$$

This equation has been used to check the consistency of the implemented thermal model.

3.5 Solar radiation pressure

Solar radiation pressure is related to the thermal recoil force since both are caused by the same physical effect, that is exchange of momentum between the spacecraft and some radiation (of course the source of radiation is different in the two cases). A model for estimating force due to SRP is implemented in the ODP and is briefly discussed in section 4.1.1. Here we note that solar flux is not exhaustively accounted for by the Solar radiation pressure model, since, as stated previously, it affects the thermal state of the spacecraft, hence its IR emission.

3.6 Geometric model and numerical implementation

The geometric model created for Pioneer includes only the major spacecraft components, that is the HGA, the RTGs, the launch ring and the spacecraft compartment bus plus the louvers radiators. All of the components have been modeled as diffuse, grey lambertian surfaces, with a minor exception for multi layer insulation. Geometry discretization and numerical solution of the heat equations have been performed thanks to a FEM software for heat transfer analysis which treats radiative heat exchange between diffuse radiators computing view factors and solving for temperature and radiosity. Calculation of thermal recoil force has been made possible thanks to the control volume (see section 3.3) added to the computational domain which is an artifact to allow for mapping of the pattern of the radiation emitted by the spacecraft.

The energy input to the system consists of three volumetric heat sources plus a surface boundary heat flux to mimic solar radiation. Two of the volumetric sources are placed inside the RTG's, the third one placed inside the spacecraft body. As a baseline case study, we have assumed that, being known the total amount of power from telemetry, and the volume of the components where the heat sources have been placed, the distribution of such sources is uniform inside the component. This is of course a

The thermal model of Pioneer spacecrafts

simplification, especially for the electrical power inside the bus, since the presence of discrete components/instrumentation inside it makes more likely the heat having some preferential. This can also be inferred by looking at the temperature readings from the six sensors placed on the platform, which indicates temperature differences up to 30°C. However, the impact of such an assumption have been addressed by performing a set of Monte Carlo simulations, as will be detailed later on.

As for the solar flux this has been applied to the concave side of the HGA and to the RTG's which are the only parts effectively exposed to it during the interplanetary cruise³.

<i>Component</i>	<i>Material</i>	ρ [kg/m ³]	κ [W/mK]	C_p [mm]	<i>Surface coating</i>	ε	α_s	
HGA	Al 6061	2770	169	961.2	front side: DC92-007 white paint	0.84	0.5	
					back side: white paint	0.04	0.17	
RTG body	HM31A-F Mg	1800	104.6	1047.6	white paint	0.82	(0.50) 0.21	
RTG fins	HM21A-T8 Mg	1800	136.6	1047.6	white paint	0.82	(0.50) 0.20	
S/C body	Al 6061	2770	169	961.2	MLI: aluminized Mylar/Kapton	0.69	0.20/ 0.46	
					Louvers: bare	$f(x,t)$	-	
ALR	Al 6061	2770	169	961.2	Interior	black paint	0.84	0.95
					Exterior	bare	0.10	0.24

Table 1: Thermo-optical properties of main Pioneers' surfaces.

Thermo-optical properties of material and surfaces have been retrieved from (TRW Systems, 1971), relevant ones are reported in Table 1. The values of emissivity and solar absorptance are BOL values. Actually one may expect a surface degradation due

³ The inclination Pioneer 10 orbit to the J2000 ecliptic after Jupiter encounter was $\approx 3^\circ$, while inclination for Pioneer 11 after Saturn encounter was $\approx 16^\circ$, moreover at heliocentric distances Sun and Earth direction are quite similar, so one can assume that the direction of the incoming Sun flux is approximately parallel to HGA axis.

to exposure to UV radiation, charged particles or contaminating particles. The general result is an increase in solar absorptance with negligible effect on the emissivity, unless severe deposition of “dust” occurs such to sensibly modify the surface coating (Gilmore, 2002) for example reports $\alpha_s = 0.5$ for EOL emissivity of white painted surfaces. White paint absorptance is reported to undergo an increase from 0.20 up to 0.60 in few years of mission.

An important fraction of the total heat rejected off the spacecraft is radiated by the louvers. A choice has been made for modeling the louvers without adding to the model physical components for the blades, springs, platform, it has been rather preferred to simulate their presence by specifying over a region surrounding the launch ring, a variable emissivity function of the temperature and spatial coordinates.

In doing so, no attempt has been made to retrieve the exact values of the area and emissivity of the blades from design documentation, it has been preferred to use as main information the amount of heat dissipated by the louver system as a whole, as reported in Figure 5 taken from (Slava G. Turyshev & Toth, 2008). It has been therefore possible to extrapolate a law for emissivity variation, which results in:

$$\varepsilon_{louver} = 0.01 + 0.58 - \frac{0.38}{1 + \exp(0.35(T - 288))} \exp(-10|x^2 + z^2 - 0.4^2|) \quad (4-21)$$

The kind of the functions used in (4-21), S-shaped exponential for temperature, Gaussian “bell” shape for spatial coordinates are instead an arbitrary choice made to avoid sharp discontinuities.

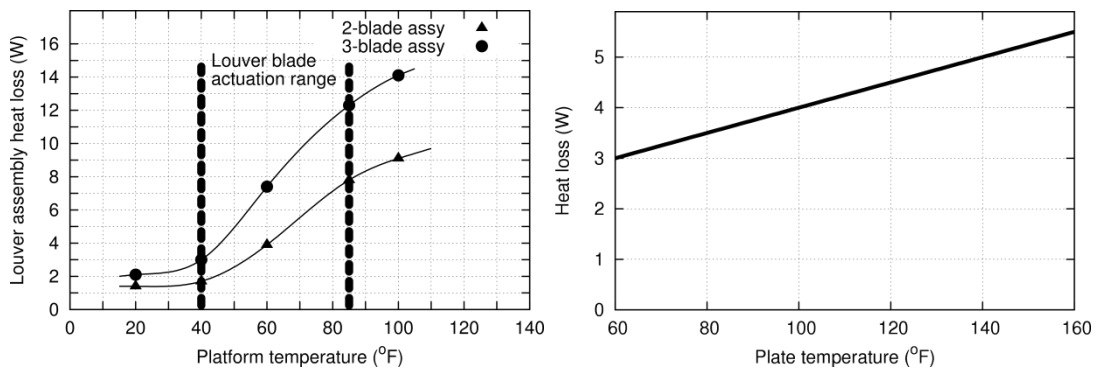


Figure 4: Heat dissipated by louvers blade assemblies (left) and louvers structure (right) from design documentation.

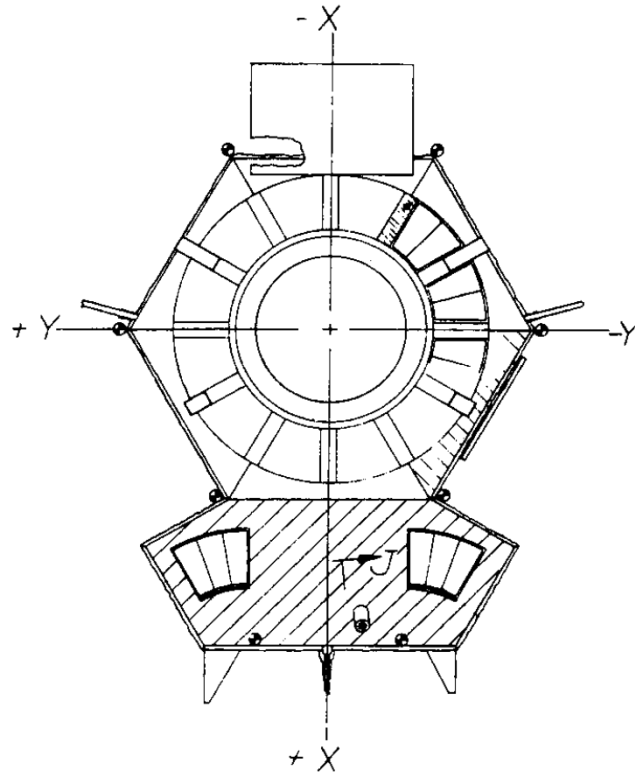


Figure 5: Louvers arrangement on bus, taken from (TRW Systems, 1971).

Outside of the temperature actuation range the emissivity is kept fixed, which seems a quite reasonable assumption. The numeric constants in the formula have been tuned in order to match the value of the power extrapolated from , at four measurement temperatures. This is equivalent to prescribe the value of $\int \epsilon dA$ according to the table below:

Temperature [K]	Total heat loss [W]	$\int \epsilon dA = \frac{W}{\sigma T^4}$ [W/K ⁴]
266	20	0.07
278	30	0.09
288.7	64	0.16
303	124	0.26

These leads to louver *equivalent* emissivity of 0.21 in fully closed configuration and 0.58 in fully open condition. These numbers are somehow in disagreement with data found on Ref. PC-202 itself, which reports $\epsilon = 0.04$ for the blades, and 0.82 for the

radiating platform underneath. In this regards we explicitly note that the area integral of eq. (4-21) is highly dependent on the kind of mesh and finite elements used in the FEM model, therefore it works only for the specific model developed. In other words, the relevant physical data for the model is $\int \varepsilon dA$, while the value of the emissivity alone is intimately related, and a consequence, of the discretized geometry implemented. The inconsistency of the model is therefore only apparent. Once again it is noticed that the driving criteria in this kind of model is the preservation of the total power emitted by the louvers according to design documentation rather than matching of detail geometry, surface area or emissivity alone.

3.7 Simulations set up and convergence check

All surfaces are active radiating ones, with boundary condition specified by eq. (4-11), except for concave side of HGA and for RTG's which are subjected to an additional inward heat flux equal to:

$$q_s = \frac{1366}{d^2} \alpha_s n_y \quad (4-22)$$

As a side note, we point out that the solar flux inside the thermal model introduces in principle a dependency on the thermal recoil force on the actual trajectory followed by the spacecraft (via the heliocentric distance d) which in turn depends on the TRA itself. As said spacecraft geometry is surrounded by a control volume, a perfect blackbody at 0K temperature whose function is to detect incoming radiation. Thermal recoil force is computed as the following surface integral:

$$TRF = \frac{W_Z}{c} = \frac{1}{c} \int_{CV} H \hat{z} \times \hat{n} dS \quad (4-23)$$

Where n is the surface normal versor. Numerical consistency of the model has been checked using energy conservation as stated in eq. (4-20). Results indicates that while the first equality is always satisfied (difference below 10^{-7} W) the second equality gives residuals from 2 to 3 Watts approximately, which is on the order of 0.1% of the total input power. This is to be expected because of the highly different sizes of spacecrafts components w.r.t. the CV making the computation of view factors a not very well posed numerical problem.

The thermal model of Pioneer spacecrafts

If one assumes this energy unbalance having no preferred direction, discrepancy per unit solid angle is $3W/4\pi \approx 0.23 W$. This value can be assumed as a figure of merit of the numerical error affecting the computed directional radiated power.

Figure 7 and Figure 8 display some relevant outputs of the thermal model. In Figure 7 the radiation reflected by the HGA is shown where the contribution from the RTG's is clear in the peripheral region of the dish (which is projected in 2D). Also some radiation coming from the hexagonal bus is also evident. Figure 8 shows the radiation by the aft side of the bus where a circular region of high radiative power is evident in the region where louvers are simulated.

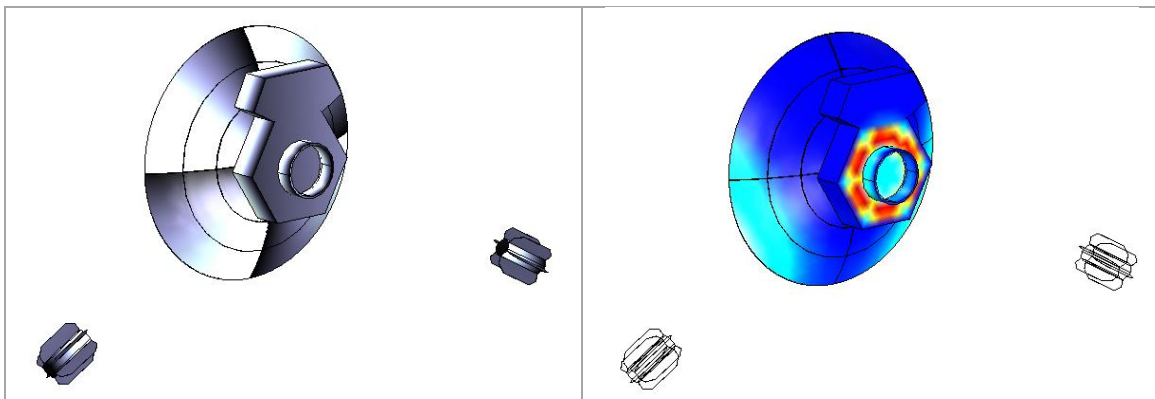


Figure 6: geometry model (left) and sample plot of emitted radiation from Pioneers thermal analysis⁴.

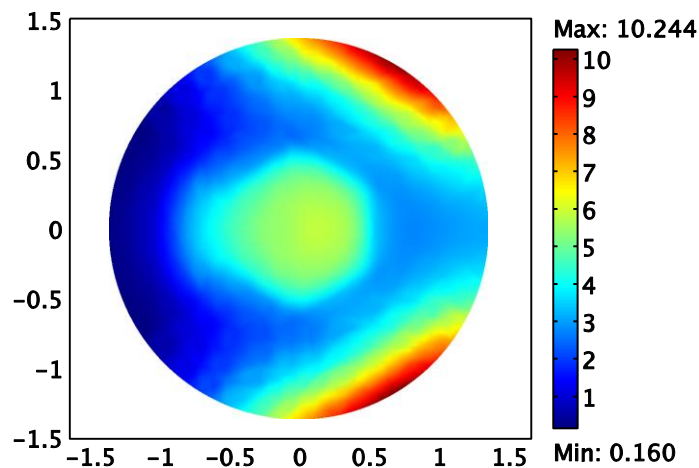


Figure 7: irradiation reflected by HGA back-side taken from a sample thermal simulation. Contribution from RTG's heat on two edge regions is evident.

⁴ RTG's on right figure are not colored because their high emission goes out of scale.

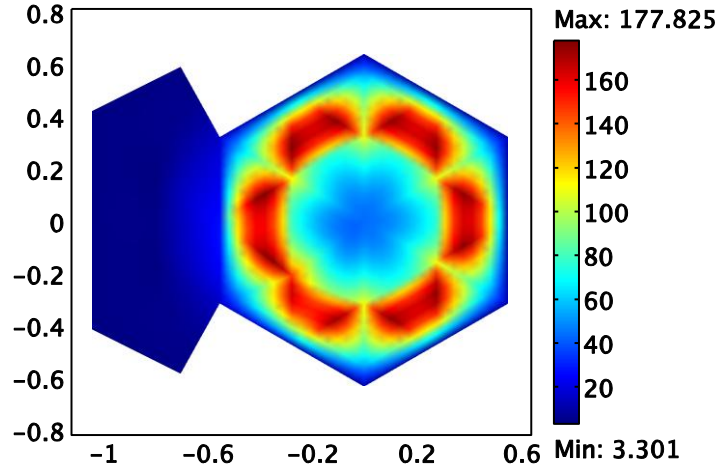


Figure 8: radiosity emitted by the back side of the compartment bus, taken from a sample thermal simulation. Contributions from heat rejected by louver is indicated by the red annular region.

3.8 Sensitivity analysis

The knowledge of several parameters of the spacecraft thermal model is quite inaccurate and sensitivity of the solution to such parameters shall be addressed. First we may think about the thermo-optical properties of the surfaces, i.e. emissivity and solar absorptance. As a result many years of interplanetary cruise during which the spacecraft is exposed to charged particles, UV radiation and dust, its surface conditions may undergo severe degradation. Another uncertain in the model comes from the distribution of the internal power inside the RTG's and the main bus, since only the amount of power is known. This is especially true for the electrical power since this is dissipated inside discrete components/instrumentations and the assumption of power uniformly distributed inside the volume of the bus can be quite inaccurate.

To address the impact that errors in the knowledge of such parameters may have on the estimation of the TRF, a Monte-Carlo-like approach has been followed.

To simulate the variation in volumetric heat sources distribution functions inside the RTG's and spacecraft bus, the following (arbitrary chosen) sinusoidal functions have been used:

$$Q_{el}(x, y) = \bar{Q}_{el} [1 + A_x^B \sin(2\pi x/L_x^B + \varphi_x^B) + A_y^B \sin(2\pi y/L_y^B + \varphi_y^B)] \quad (4-24)$$

$$Q_{th}(x) = \bar{Q}_{th} [1 + A_x^R \sin(2\pi x/L_x^R + \varphi_x^R)]$$

Where L_x^B L_y^B are characteristic dimension of the spacecraft main bus in x and y directions, L_x^R is the RTG's axial length.

For each simulation, A_x^B , A_y^B , A_x^R are samples drawn uniform distributed numbers inside the open interval (0,1); φ_x^B , φ_y^B , φ_x^R are samples drawn from uniform distributed numbers inside (0,2 π); \bar{Q}_{el} and \bar{Q}_{th} are volumetric heat coefficients related to the total thermal and electrical powers such that the following relations hold:

$$P_{el} = \int_{Bus} Q_{el} dV_B \quad P_{th} = \int_{RTG} Q_{th} dV_R \quad (4-25)$$

Solar absorptance of HGA and RTG's has been varied

$$\alpha_S = \bar{\alpha}_S + d\alpha_S \quad (4-26)$$

Where $\bar{\alpha}_S$ is the nominal absorptance set equal to 0.4 and $d\alpha_S$ are samples drawn from uniform distributed numbers inside (-0.1, 0.1).

Uncertainty in surfaces emissivity coefficients has been accounted for as follows:

$$\varepsilon_i = \bar{\varepsilon}_i + d\varepsilon_i \quad (4-27)$$

Where $\bar{\varepsilon}_i$ is the nominal emissivity of the i -th modeled surface and $d\varepsilon_i$ are samples drawn from uniform distributed numbers inside (-0.15 $\bar{\varepsilon}_i$, 0.15 $\bar{\varepsilon}_i$).

3.9 Fitting of Monte Carlo Simulations

In order to be incorporated in the OD program, the results of MC simulations have to be converted to an acceleration in the time domain which can be represented in the ODP (i.e. polynomials up to the 4th order and exponential function). In such a way TRA is represented with a finite number of parameters and their associated covariance matrix.

Two different approaches have been taken under consideration to perform the fitting; one way is to include the variability of magnitude of power in the process of MC simulations. In this approach, different series of MC are performed, each for a certain point in the trajectory (identifiable by the heliocentric distance, e.g. 20 AU). For each trajectory point, thermal and electrical power are nominally known from telemetry. To simulate uncertainty, white noise is added to nominal values (see expressions for heat sources strength, Q_{el0} and Q_{th0}). Then for each trajectory point a mean value of TRF is computed together with its standard deviation, representing variation due to all uncertainty parameters considered simultaneously. In other words, the simulations are split into subgroups, one for each trajectory point. Finally, a LSQ fitting of the TRF acting on the probe along its trajectory is performed. This approach, which is quite

straightforward, has however the drawback of using a relatively limited amount of data to generate the function $TRF=f(t)$; having a limited amount of points to perform the fit, the confidence of the fitting is relatively poor.

A second, more sounding approach relies on the consideration that it is reasonable to expect the directionally radiated power, $W_Z=TRF \times c$, being a linear function of the energy input to the system. This is in turn represented by thermal and electrical powers *inside* the spacecrafts, plus the solar flux impinging *on* the spacecraft.

One can then seek for a regression of the MC simulations output of the kind:

$$W_Z = x_1 P_{th} + x_2 P_{el} + x_3 \tilde{\Phi}_S$$

Where the solar flux Φ_S varies inversely proportional to the squared distance of the probe to the Sun in astronomical unit, as: $\Phi_S=1366/AU^2$ W/m². To preserve homogeneous dimensions, we have introduced a ‘‘Solar power’’ $\tilde{\Phi}_S = \pi D_{HGA}^2 \Phi_S$ equal to the flux times the projected surface of the HGA.

Goodness of the linear fitting assumption is verified a posteriori by inspection of post-fit residuals, which have a standard deviation of 4.5W , while the mean is 0.1W (remember that the order of magnitude of the anisotropic power is on the order of few tens of Watt). The mean being on the order of 2% of the standard deviation indicates that the fitting function is well chosen.

We note here that if we could neglect the contribution due to the solar flux, then the fitting could be performed regardless of the particular point in the trajectory corresponding to the couple (P_{th}, P_{el}) . This second approach is the one followed in the present work. The fitting has been performed using classical least squares techniques with consider parameters. The basis of the theory will be recalled in the following, focusing on the aspects relevant for our application.

A linear observational model is given by:

$$\mathbf{z} = \mathbf{H}\mathbf{x} + \mathbf{v} \quad (4-28)$$

where:

\mathbf{z} is the $m \times 1$ vector (m being the number of MC simulations performed) of the computed recoil force $TRF = W_Z/c$;

$\mathbf{x}=[x_1 \ x_2 \ x_3]^T$ is the $n \times 1$ vector ($n=3$) of the unknown fitting coefficients;

$\mathbf{H}=[\mathbf{P}_{th} \ \mathbf{P}_{el} \ \tilde{\Phi}_S]$ is the $m \times n$ observation matrix (\mathbf{z} , \mathbf{P}_{th} , \mathbf{P}_{el} and $\tilde{\Phi}_S$ are column vectors whose length equals the number of MC simulations performed);

The thermal model of Pioneer spacecrafts

\mathbf{v} is the $m \times 1$ vector of observational noise; in our case by “noise” we consider the scatter in the TRF introduced by the uncertain parameters of the MC simulations. The theory summarized below relies on the assumption of \mathbf{v} being a white Gaussian noise leading to an unbiased estimate.

An \mathbf{x} vector is sought to minimize the weighted sum of squared residuals:

$$\mathbf{J} = (\mathbf{z} - \mathbf{H}\mathbf{x})^T \mathbf{R}_Z^{-1} (\mathbf{z} - \mathbf{H}\mathbf{x}) \quad (4-29)$$

\mathbf{R} being the measurement error covariance matrix (symmetric, positive defined). In doing so, we do not account for possible a-priori information on the state (usually indicated as \mathbf{x}_0) and on its covariance.

The weighted least-square best fitting is then given by:

$$\mathbf{x} = (\mathbf{H}^T \mathbf{R}_Z^{-1} \mathbf{H})^{-1} (\mathbf{H}^T \mathbf{R}_Z^{-1} \mathbf{z}) \quad (4-30)$$

While the formal covariance matrix of the estimate is defined as:

$$\Gamma_{\mathbf{x}} = E[\delta\mathbf{x}\delta\mathbf{x}^T] = (\mathbf{H}^T \mathbf{R}_Z^{-1} \mathbf{H})^{-1} \quad (4-31)$$

where E denotes the expectation operator and $\delta\mathbf{x}$ is the error of estimation.

In our case we set $\mathbf{R}_Z = \text{diag}(1/\sigma_Z^2)$ with σ_Z is a value tuned in order to match post-fit residual *rms* value such that:

$$\mathbf{J} = \sum_{i=1}^m (z_i - H_{ij}x_j)^2 \approx m \quad (4-32)$$

With this choice of \mathbf{R}_Z we weight all the data at in the same way (there is no reason to trust some MC simulations more than others) and we scale its norm as to compute the correct value of $\Gamma_{\mathbf{x}}$, that is, the confidence bounds of our estimate. Fitting results are reported in Table 2.

Estimated \mathbf{x}	Estimated $\sigma_{\mathbf{x}}$	Normalized covariance $\Gamma_{\mathbf{x}}$
0.0132	1.76×10^{-4}	$\begin{bmatrix} 1 & -0.905 & 0.195 \\ 0.905 & 1 & -0.478 \\ 0.195 & -0.478 & 1 \end{bmatrix}$
0.553	8.17×10^{-3}	
-0.207	9.02×10^{-3}	

Table 2: Estimated coefficients and formal covariance of the linear regression of thermal recoil force w.r.t input power sources.

The covariance matrix globally accounts for uncertainty in internal distribution of thermal power inside the RTGs and the electrical power *inside* spacecraft body, as well as uncertainty in surface optical properties and, finally, the goodness of the assumed linear fitting function for the thermal recoil force.

Up to now we have assumed the elements of H matrix being “exact”. This is true while performing the fit in the power domain, since these are the input of the thermal simulations. However, when mapping the results to the time domain, one relies on the knowledge of the variation of thermal, electrical and solar power through the trajectory, and this data are affected by errors. As reported in (V. Toth & Turyshev, 2009) telemetered power readings are affected by uncertainties of 2.1 and 1.8 W for thermal and electrical power respectively: these figures account for limited telemetry resolution and uncertainty in the values reported in Figure 9 which are rounded off to the nearest integer Watt. Moreover the actual solar power reaching the spacecrafts differs in general from the value used for the simulations due to variation in solar activity and inaccuracy of the assumed law for Φ_S variation. A simple way to account for this is by assuming uncertainty on the solar flux constant at 1 AU (1366 W/m^2): a value of 5 W has been assumed, guessed from the variability of solar constants data published by different sources.

Inclusion of such sources of error can be accomplished applying the theory of linear estimation in presence of the so called consider parameters. That is, we consider the observation matrix being function of a vector of known parameters, \mathbf{y} , affected by an uncertainty represented by a covariance matrix R_y .

The underlying theory, briefly summarized, is taken from (Moyer, 1971), in order to be consistent with the estimation filter implemented in the ODP, in the effort of properly integrating the thermal model of the spacecraft to the process of orbit determination.

We shall consider an augmented vector $\mathbf{q}=[\mathbf{x} \ \mathbf{y}]^T$ and a new cost function:

$$\mathbf{J} = (\mathbf{z} - \mathbf{H}\mathbf{x})^T \mathbf{R}_z^{-1} (\mathbf{z} - \mathbf{H}\mathbf{x}) + (\mathbf{y} - \mathbf{y}^*)^T \mathbf{R}_y^{-1} (\mathbf{y} - \mathbf{y}^*) \quad (4-33)$$

where \mathbf{y} and \mathbf{y}^* are the *a-priori* and the *exact* value of the vector of estimated parameters. In our case, every element of H is a consider parameter, and we can build \mathbf{y} as the following column vector of length $n \times m$:

$$\mathbf{y} = [h_{11} \dots h_{1n} \ h_{21} \dots h_{2n} \ h_{m1} \dots h_{mn}]^T = \quad (4-34)$$

Since there is no estimate on \mathbf{y} , it holds that $\mathbf{y} \equiv \mathbf{y}^*$. Therefore the cost function remains unchanged. As a consequence, the estimate of \mathbf{x} is unchanged as well. The presence of R_y however affects the value of the covariance matrix. It can be shown that (Moyer, 1971):

$$\begin{aligned} \Gamma_{\text{tot}} &= E[\delta \mathbf{q} \delta \mathbf{q}^T] = \\ &= (\mathbf{H}^T \mathbf{R}_Z^{-1} \mathbf{H})^{-1} + \\ &(\mathbf{H}^T \mathbf{R}_Z^{-1} \mathbf{H})^{-T} (\mathbf{H}^T \mathbf{R}_Z^{-1} \mathbf{A}_y) \mathbf{R}_y (\mathbf{A}_y \mathbf{R}_Z^{-1} \mathbf{H}) (\mathbf{H}^T \mathbf{R}_Z^{-1} \mathbf{H})^{-1} \end{aligned} \quad (4-35)$$

where the matrix \mathbf{A}_y is given by:

$$\mathbf{A}_y = \left[\frac{\partial \mathbf{z}}{\partial \mathbf{y}} \right] = \begin{bmatrix} \mathbf{x}^T & 0 & \dots & 0 \\ 0 & \mathbf{x}^T & & \vdots \\ \vdots & & \ddots & 0 \\ 0 & \dots & 0 & \mathbf{x}^T \end{bmatrix} \quad (4-36)$$

The two addends on the right hands side of eq. (4-35) represent the two contributions to the total covariance, Γ_{tot} : without the presence of consider parameters, Γ_{nc} , (i.e. covariance found in eq. (4-31)) and with consider parameters, Γ_{con} , such that:

$$\Gamma_{\text{tot}} = \Gamma_{\text{nc}} + \Gamma_{\text{con}} \quad (4-37)$$

Integration of thermal model in the ODP requires mapping of the fitting coefficients to the time domain. Pioneer RTG's thermal power, P_{th}^* have been measured just prior to launch as reported in the following table taken from (Slava G. Turyshev & Toth, 2008):

RTG#	Spacecraft	Location	Test date	Thermal power (W)
44	Pioneer 10	Outboard	Oct 1971	649
45	Pioneer 10	Inboard	Nov 1971	646
46	Pioneer 10	Outboard	Nov 1971	647
48	Pioneer 10	Inboard	Dec 1971	649
49	Pioneer 11	Outboard	Sep 1972	649
51	Pioneer 11	Inboard	Oct 1972	650
52	Pioneer 11	Outboard	Oct 1972	649
53	Pioneer 11	Inboard	Oct 1972	649

Figure 9: Pioneer 10&11 RTG's power measured prior to launch, taken from (Slava G. Turyshev & Toth, 2008)

This power is expected to decay with a half time of 87.4 years, that is:

$$P_{th}^* = P_{th}^*(t_0) \times 2^{-(t-t_0)/87.4} \quad (4-38)$$

We denoted this quantity with a * since what we actually need is the thermal power after the electrical energy is removed from it, that is: $P_{th} = P_{th}^* - P_{el}^*$

Such information can be retrieved thanks to the telemetry readings of voltage and current drawn off each RTG. Actually, P_{el}^* is not entirely dissipated inside the spacecraft bus, but part of it is dissipated from instrumentation placed outside, and other sources. These aspects are deeply discussed in (V. Toth & Turyshev, 2009) and (Slava G. Turyshev & Toth, 2008) where a diagram of the net powers P_{th} and P_{el} for Pioneer 10 is found and reported here in Figure 10. These have been fitted with quadratic polynomials of time.

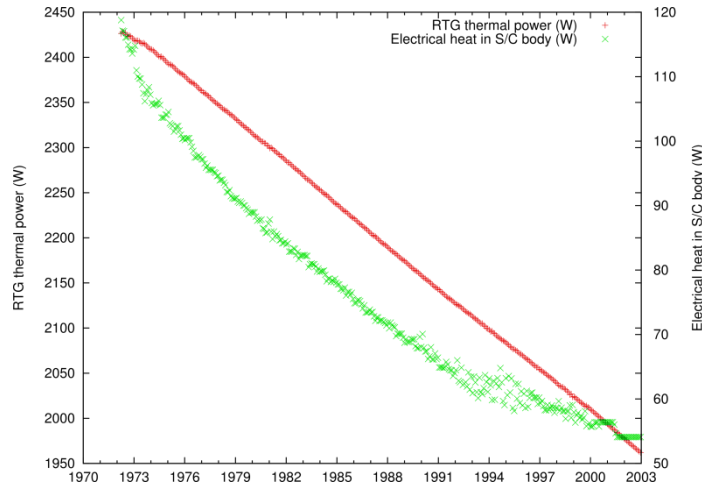


Figure 10: Pioneer 10 RTG's thermal power (red curve) and electrical power dissipated inside S/C bus retrieved from telemetry, taken from (Slava G. Turyshev & Toth, 2008).

As for Pioneer 11, only P_{el}^* is available at the moment, and since this is almost identical to the corresponding values for Pioneer 10, we have been chosen to use the same fit also for Pioneer 11, only shifting the initial time t_0 to one year later.

The same is applied for the solar flux input, which is approximately proportional to the inverse of the heliocentric distance squared; this last grows almost linearly in time during interplanetary cruise, the exact variation is retrieved from orbital solutions for Pioneer 10 and 11. This led to the following expression for thermal recoil acceleration:

$$TRF(\tau) = \frac{W_Z}{c} = A_{TRF} + B_{TRF}\tau + C_{TRF}\tau^2 + G_{1TRF}e^{-\beta_1\tau_1} + G_{2TRF}e^{-\beta_2\tau_2} \quad (4-39)$$

The thermal model of Pioneer spacecrafts

	Estimated ξ	Estimated σ_ξ	Normalized covariance Γ_ξ
A_{TRF} [N]	3.072×10^{-7}	2.11×10^{-9}	$\begin{bmatrix} 1 & -0.965 & 0.956 & -0.621 & -0.621 \\ -0.965 & 1 & -0.99 & 0.498 & 0.498 \\ 0.956 & 0.956 & 1 & -0.488 & -0.488 \\ -0.621 & 0.498 & -0.488 & 1 & 1 \\ -0.621 & 0.498 & -0.488 & 1 & 1 \end{bmatrix}$
B_{TRF} [N/s]	-2.443×10^{-16}	3.14×10^{-8}	
C_{TRF} [N/s ²]	1.033×10^{-25}	1.54×10^{-27}	
G_{1TRF} [N]	-6.61×10^{-8}	2.95×10^{-9}	
G_{2TRF} [N]	-1.762×10^{-8}	7.86×10^{-10}	
β_1 [1/s]	2.267×10^{-8}	-	
β_2 [1/s]	4.319×10^{-9}	-	

Table 3: Fitting coefficients and covariance of Pioneer 10 thermal recoil force as a function of time.

In the above equation the polynomial accounts for the on board contribution to radiation force, while the exponentials for the solar flux contribution; τ is seconds past launch; $\tau_1 = \tau_2 =$ seconds past 16st July 1975 (fit of heliocentric distance starts after Jupiter encounter). Actually the exponential fit is applicable only to Pioneer 10 trajectory while, for Pioneer 11, two 4th order polynomials have been used for fitting the two segments of trajectory covered by tracking data, *pre* and *post* Saturn encounter. The subsequent discussion will be limited, for the sake of brevity, to the temporal fit of Pioneer 10 represented by eq. (4-39)⁵.

Mapping of the consider covariance from “power” domain to time domain can be accomplished with an orthogonal transformation, that is, a change of variables from \mathbf{x} to $\xi \triangleq [A_{TRF} \ B_{TRF} \ C_{TRF} \ G_{1TRF} \ G_{2TRF}]^T$:

$$\mathbf{x} \rightarrow \xi(\mathbf{x}) \tag{4-40}$$

Such that:

$$\delta \mathbf{x} = N \delta \xi \tag{4-41}$$

⁵ Pioneer 11 thermal recoil force has been fitted as:

$$A_{TRF} + B_{TRF} \tau + C_{TRF} \tau^2 + A_{\varphi_i} + B_{\varphi_i} \tau_i + C_{\varphi_i} \tau_i^2 + D_{\varphi_i} \tau_i^3 + E_{\varphi_i} \tau_i^4 \quad i=1,2$$

with $\tau =$ seconds past launch; $\tau_i =$ seconds past 1st September 1977 (up to τ_2); $\tau_2 =$ seconds past 12th January 1980.

$$N \triangleq \frac{\partial \xi}{\partial \mathbf{x}} = \begin{bmatrix} A_{th} & A_{el} & 0 \\ B_{th} & B_{el} & 0 \\ C_{th} & C_{el} & 0 \\ 0 & 0 & G_1 \\ 0 & 0 & G_2 \end{bmatrix}$$

By definition of covariance matrix:

$$\Gamma_{\xi} \triangleq E[\delta \xi \delta \xi^T] = N E[\delta \mathbf{x} \delta \mathbf{x}^T] N^T \quad (4-42)$$

Values of the force coefficients in eq. (4-39) and relative covariance are displayed in table

Covariance just computed is referred to TRF; the covariance of the acceleration TRA cannot be computed simply by dividing the coefficients in ξ and N by the spacecraft mass, since this last is also a consider parameter⁶. Therefore another change of variable is required.

If we define:

$$\chi \triangleq M \xi = M [A_{TRF} \ B_{TRF} \ C_{TRF} \ G_{1TRF} \ G_{2TRF}]^T$$

where $M = \text{diag}(1/m_{Pio})$, then we are willing to compute the covariance of χ :

$$\Gamma_{\chi} \triangleq E[\delta \chi \delta \chi^T] = M \delta \xi \delta \xi^T M^T + \delta M \xi \xi^T \delta M^T = \frac{1}{m_0^2} \Gamma_{\xi} + \delta M \xi \xi^T \delta M^T$$

The first term on RHS is simply the previously computed covariance of χ divided by the nominal mass squared, that is, covariance of TRA when mass is perfectly known.

As for the second term, (which accounts for uncertainty in mass) differentiation of M matrix leads to:

$$\Gamma_{\chi} = 1/m_0^2 \Gamma_{\xi} + \frac{\sigma_m^2}{m_0^4} \xi \xi^T \quad (4-43)$$

Where σ_m is the mass uncertainty assumed equal to 9 kg and nominal mass m_0 have been set equal to 246.4 and 235.9 Kg for Pioneer 10 and Pioneer 11 respectively (see discussion in section 4.1.1).

We mentioned in section 3.1 that IR emission is not the only kind of energy radiated into space by Pioneer, since there is also the power, nominally 8W, carried by the

⁶ Mass is not telemetered during the mission (see section 4.1.1)

highly collimated radio beam transmitted by the HGA. This aspect is discussed in (Scheffer, 2003) where an efficiency of the conversion from power to linear momentum of 0.83 is computed. This value has been used in the present study as well. The resulting force act in sunward direction, thus it has to be subtracted to the constant term, A_{TRA} , of the recoil acceleration just computed. In this way we get to a sort of global radiation recoil acceleration, which is the ultimate output which has been integrated to the orbit analysis discussed hereafter. Time evolution of total radiative recoil force is depicted in Figure 11.

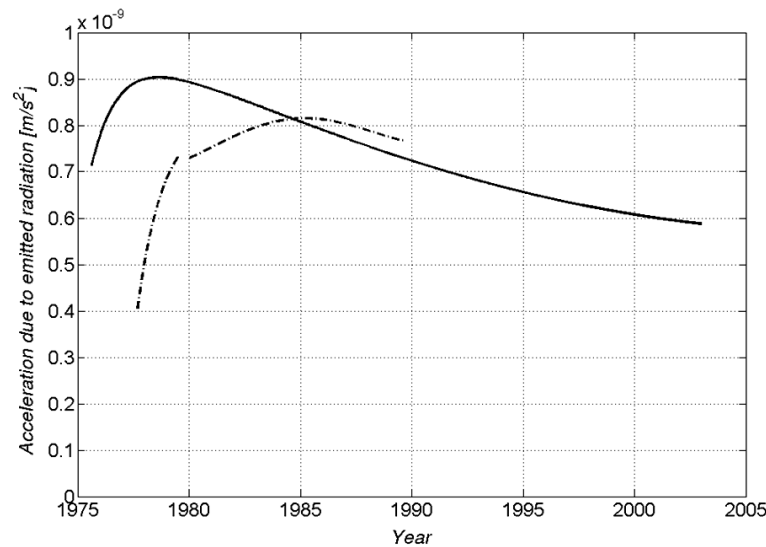


Figure 11: Acceleration due to emitted radiation by Pioneer10 (full line) and Pioneer 11 (dash-dot line) along the part of trajectories covered by analyzed tracking data. Spot in Pioneer 11 corresponds to Saturn fly-by.

Pictures show clearly that TRA is not decreasing monotonically in time. In fact, by looking from right to left we see that TRA increases because of the increase in available power, but continuing towards smaller heliocentric distances, the effect of the solar flux (which subtracts to the contributions from RTG's heat reflected by the HGA backside and heat rejected by the louver system) grows and becomes dominant w.r.t. the increase in onboard power, thus inverting the temporal trend of the acceleration. We note that maximum recoil acceleration occurs for Pioneer 10 at approximately 16 AU, while for Pioneer 11 at ≈ 19 AU. Moreover, maximum value of recoil force for Pioneer 11 is lower than for its predecessor since Pioneer 11 resided longer within the Solar System due to its second planetary encounter (at Saturn): as a consequence it reached distances

where effect of solar flux was negligible later in its operational life, when the onboard power had already sensibly decreased.

Summarizing the results presented in this chapter, we highlight that in the approach followed the accuracy of the thermal model is addressed by building up the formal covariance of the fitting coefficients in different steps. Several (hopefully all the relevant) sources of error affecting TRA computation have been taken into account.

Eq. (4-39), and the corresponding one for Pioneer 11, can be regarded as the overall output of the thermal analysis to be fed as an input dynamic model input to the orbit determination process which affects spacecraft trajectory.

Orbit analysis of radiometric data

This chapter begins with a presentation of the concepts underlying spacecraft navigation and orbit determination. Then it proceeds with a brief description of the software used for analyzing Pioneers radiometric data, the ODP. This chapter is absolutely not intended to be a complete survey of these topics: this is far beyond the scope of this thesis author's capacity. It rather aims at providing a minimum background context to the subsequent matters, that is, the strategies used for processing Doppler data will be presented focusing on two different approaches used, *singe-arc* and *multi-arc* chapter.

4.1 Spacecraft navigation and orbit determination via the ODP

The main objective of spacecraft navigation is to determine and predict the position and velocity of a spacecraft (orbit determination) and to modify its velocity such that actual orbit matches up with the target one (flight path control).

Orbit determination is usually accomplished by performing several kind of radio-tracking measurements, most commonly range and Doppler measurements, which rely on a radio link between the spacecraft and the Earth. Processing of the received tracking data is then required for reconstructing the trajectory: the computational tool used for this task during this study is NASA-JPL's ODP (*Orbit Determination Program*). This software includes a model of Solar System dynamics which implements the relativistic equations of motion for a spacecraft subject to gravitational and non-gravitational accelerations, and integrates them to obtain spacecraft's trajectory. Based on the computed trajectory, it further computes the radio signals sent by the probe to the

tracking stations on Earth (*observed observables*). The difference between the *observed* and *predicted* values (the so called *residuals*) is then fed to a recursive filter in order to improve the knowledge of a certain set of parameters affecting the dynamics of the spacecraft (*solve-for* parameters). Such parameters must include the initial conditions of the spacecraft; other parameters may be gravitational harmonics of celestial bodies, or maneuvers intensities.

Previously reported orbital solutions for Pioneer 10 required the addition of a constant sunward acceleration to those coming from the implemented dynamical models, both of gravitational and non-gravitational origin. Such additional acceleration has become known as the *Pioneer Anomaly*.

From this brief, high level description of the ODP, three main steps can be identified which shall be accomplished:

1. Trajectory propagation
2. Observables generation
3. Parameter Estimation

4.1.1 Dynamical models

Trajectory propagation requires integration of equation of motion of the spacecraft subjected to a number of forces which can be grouped into:

1. *Gravitational* forces:
 - Central body force (Keplerian point-mass)
 - Secondary bodies forces (Keplerian point-mass)
 - Central body higher order gravity harmonics
 - Relativistic effects
2. *Non gravitational* forces
 - Solar radiation pressure
 - Aerodynamic drag
 - Propulsive forces (maneuvers)
 - Gas leaks

As for gravitational forces, planetary coordinates and masses are obtained using JPL's computed Ephemerides.

Not always all of the above contributions should be included in an orbit analysis. For example, for a probe in deep space cruise, higher order gravitational harmonics are surely negligible, so is the atmospheric drag.

Relevant non-gravitational accelerations during Pioneers' interplanetary cruise are originated by Solar radiation pressure and propulsive maneuvers.

The former is included as a dynamical model in the ODP in which the spacecraft components are represented with a series of geometric entities (parabolic antenna, boxes, flat plates, spheres and cylinders). Momentum exchange between photons and each component is computed as a function of its specular and diffuse reflection coefficients, and summed up. Because of the geometrical configuration of the Pioneers, having a big antenna dish constantly directed towards Earth, the only component significantly contributing to the SRP is the HGA itself which is always in a full front illumination condition, that is, only the Earth facing side of the parabolic dish is illuminated. With a simplified flat plate model, one can compute the following expression for the SRP (Jet Propulsion Laboratory Navigation Software Group, 1996):

$$a_{SRP} = \frac{[1+2(\mu_F+v_F)]\times\cos(\vartheta)}{c\times m} \frac{A\Phi_{S@1}}{d^2} \quad (6-1)$$

Where μ_F and v_F are the specular and diffuse reflective coefficients of HGA Earth facing side^{††}, which are assumed constant (i.e. degradation factors have been neglected), A is its area, m is spacecraft mass, $\Phi_{S@1}$ is solar flux at 1 AU and ϑ is the angle between the direction of the Sun and the HGA axis. Nominal value for μ_F and v_F coming from JPL calibration at early stages in the mission, are 8.055×10^{-2} , 2.757×10^{-1} for Pioneer 10 and 7.016×10^{-2} , 2.808×10^{-1} for Pioneer 11. However, as reported in (J.D. Anderson, Laing, et al., 2002), determination of these coefficients from solar acceleration inferred from tracking data is affected by errors in spacecraft mass, which is not exactly known.

As far as propulsive forces are concerned, recalling section 2.2, Pioneers spacecraft were equipped with hydrazine thrusters performing HGA re-pointing towards the Earth, delta-V maneuvers for trajectory control, and spin/de-spin maneuvers. After planetary encounters, only precession maneuvers were performed (more than one hundred in the

^{††} Reference [(J.D. Anderson, Laing, et al., 2002)] cluster the term $(1+ 2\mu_F +2v_F)$ in a single coefficient, \mathcal{K} .

years covered by the analyzed data sets). Even if precession maneuvers are expected to exert only torques on the spacecraft but no net forces, possible thrusters malfunctioning, due to, e.g., asynchronous operation of thrusters or valve leaks, may have given rise to small residual forces such that velocity jumps and or acceleration term may have occurred (see discussion in section 5.1).

Non-gravitational accelerations are mass dependant, therefore spacecraft mass must be provided as input. Pioneers masses were nearly 259 kg (223 kg of dry mass plus 36 kg of propellant) and this value is expected to decrease along the mission because of propellant consumption. However the mass is not telemetered and its value after the planetary encounters can be reconstructed only approximately. (John D Anderson et al., 1998) and (J.D. Anderson, Laing, et al., 2002) reports for Pioneer 10 mass the values of 241 and 251.8 kg, while for Pioneer 11 reported figures for the mass are 232 and 239.7 kg. In the present study the intermediate values of 246.4 and 235.9 Kg have been used as nominal masses for Pioneer 10 and 11 respectively. Uncertainty associated with such estimates has been set to $1/4^{\text{th}}$ of propellant mass, that is 9 kg and has been accounted for in the computation of the TRA as additional covariance for the polynomial coefficients (see discussion in ??). After planetary encounters Pioneer 10 and 11 underwent only precession maneuvers whose amount of propellant use is very low. Nominal performance of propulsion system, 9 g of propellant for a 3° precession as stated in (TRW Systems, 1971 page 3.4-12) suggests that overall mass consumption due to precession maneuvers should be on the order of 1 kg; even if we double this figure to include possible gas leaks, the variation is well within the uncertainty in the nominal mass value. For this reason mass has been assumed constant all over the data span for both spacecrafts.

4.1.2 Observable generations

ODP implements measurement models for calculating computed values of the observables, to be compared with the measured ones. This includes the algorithm for light-time solution between the spacecraft and the tracking station, plus media and antenna corrections for precisely modeling the propagation of tracking signals through the media in the volume between the Earth and the spacecraft. As for the light time solution, it requires precise knowledge of participants' state vectors: spacecraft's state vector is provided by the trajectory propagation facility (called DPTRAJ), while for

tracking stations accurate position in Earth fixed frame plus models of Earth's rotation and tidal motion are required. As for signal propagation the following corrections are included in the ODP which accounts for relativistic effects, i.e. speed of light reduction and light path bending due to gravitational potentials, plus media corrections. They consists of corrections due to Earth troposphere and corrections due to charged particles which can be in Earth's ionosphere, in space (interplanetary plasma) or in the Solar Corona (Moyer, 2000). Delay due to Solar Corona is computed thanks to a built in ODP model based on (the work of Anderson 1971), while other effects can be accounted for if user provides as input the zenith path delay in form of polynomials or Fourier series coefficients (Jet Propulsion Laboratory Navigation Software Group, 1996).

Effects of charged particles are said to be “dispersive”, that is they are frequency dependent. In particular, change in the optical path is inversely proportional to the square of the frequency (Moyer, 2000). S-band data are therefore highly affected by such interactions, which are usually difficult to precisely compensate, resulting in increase of noise level when, for example, a Solar conjunction occurs.

ODP further includes the possibility of correcting the computed residuals for any other possible phenomenon affecting them. As an example directly applicable to Pioneers, computed observables shall be adjusted to compensate the Doppler shift induced by spacecraft spinning (so called *Marini's effect*). This is one kind of data editing allowed to the ODP user, which include also data rejection and data weighting, as discussed in section 4.2.

4.1.3 Parameters estimation

Estimation is performed in the ODP by adjusting free parameters to minimize measurement residuals in a weighted-least-squares (WLSQ) sense^{§§}. The WLSQ filter is a linear estimator which, being applied to a non-linear problem, requires iterations in order to converge to a solution. The fundamental step of WLSQ filtering is the computation of the partial derivatives of the observations with respect to the parameters

^{§§} There is also actually a Kalman Filter-Smoother implementation for the parameter estimator which allow for inclusion of stochastic dynamical processes. Some more details will be given in section 4.5.1; WLSQ implementation will be retained as baseline case for the oncoming discussion

to be estimated, which in turn requires knowledge of the position and velocity of the participating spacecraft and tracking stations. Estimated parameters includes compulsorily spacecraft's state vector at initial time, plus optional parameters such as planetary and satellite ephemerides, gravity field characteristics, Earth station location, parameters non-gravitational acceleration models, velocity increments consequent to maneuvers. Each solve-for parameter shall be given an *a-priori value* and an *a-priori uncertainty*, which represent the available knowledge of such parameter before using the information carried by the measured data. Output of the filter will be given as the newly estimated parameters values; the formal accuracy of the estimate is an output of the filter itself in terms of an error covariance matrix. In general it is possible to include as solve-for almost all of the physical parameters which are included in the models affecting spacecraft dynamics, and/or the generation of computes observables. However, with a certain set of observed observables, raising the number of solve-for usually translates into a lower accuracy of the estimate, since convergence to a minimum of the cost function requires increasing in the solve-for a priori uncertainties.

Proper convergence of solution is usually assessed by examining post-fit residuals, which should ideally be randomly Gaussian distributed, or, at least, should not exhibit distinctive deterministic signatures (trends) and should have a sufficiently small μ/σ ratio (say on the order of 10^{-2}). There are also other criteria to verify consistency of solution related to ODP filter implementation are, these are discussed in section 4.3.

Besides the *solve-for* parameters, the filter is capable of managing the so called *consider* ones, that is, some model parameters which are quite accurately modeled, but whose uncertainties sensibly affect the covariance of the solve-for. In particular, the consider covariance increase the uncertainty of the standard solution, however without altering the solution itself. Typical consider parameters may be e. g. Earth Stations coordinates, coefficients of media calibration, optical properties of spacecraft components.

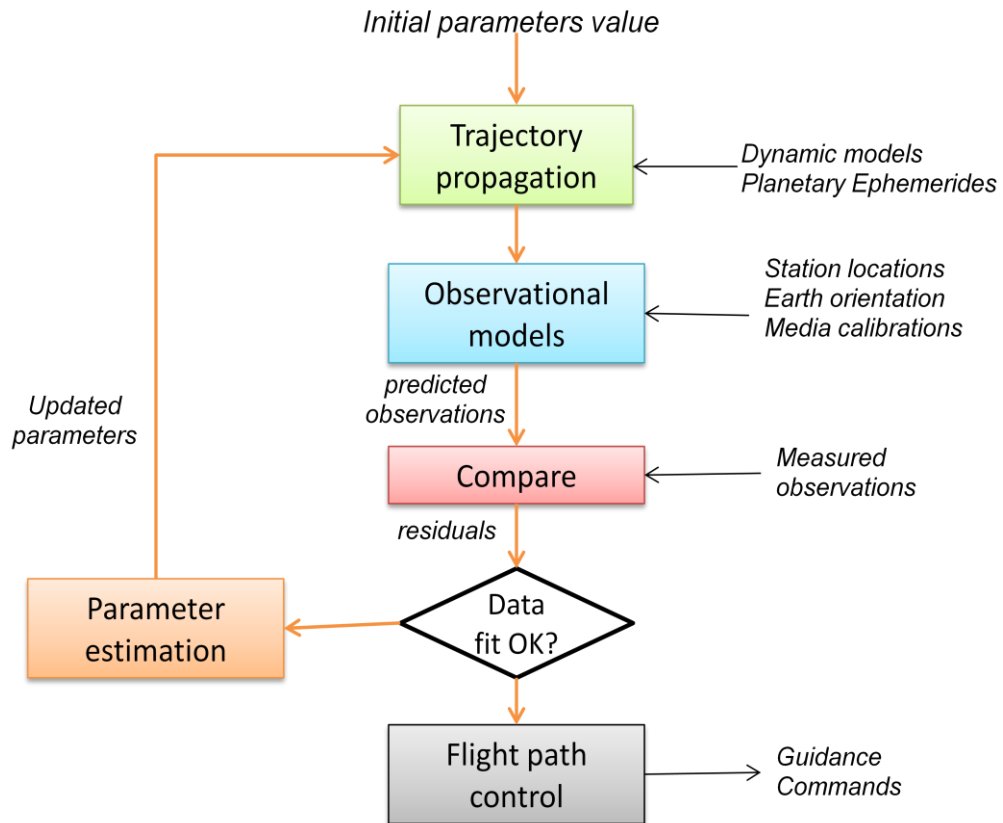


Figure 12: Schematics of the process of orbit determination.

4.2 ODP subroutines

In this section the discussion of 4.1 and 4.3 will be related to the ODP implementation. The capabilities of the program in terms of spacecraft navigation goes beyond the aspects which have been exploited during the analyses of Pioneers data: the description of the subprograms which follows is intentionally limited to the aspects covered during this project.

The iterative procedure for parameters estimation seen in previous chapter is a highly complex task, and the ODP is conveniently divided into several sub-programs, each one demanded to a specific step of the orbit determination process, so that the overall process results a bit more user-friendly. Each of the subprograms may receive input files which belongs to one of the following two kinds:

- *Binary* files with extension *.nio**** which are in a machine readable format but can be translated to text files by a dedicated routine.

*** *nio* stands for Navigation Input/Output format.

- *Namelist* files, text files created by the user in which all the aspects of the orbit analysis to be performed are specified by the user, following a predefined syntax.

The output is again a binary file *.nio*, which can be translated into human readable text file thanks to a dedicated routine.

A standard run of the ODP program can be therefore requires execution of following programs:

GINUPDATE: updates a *gin.nio* file following instructions included in a namelist *gin.nl*. The output *.nio* basically includes a global description of the models for probe dynamics and observable computations (sometimes these are globally referred to as the “model of the Universe”). Relevant namelist input include:

- S/C geometry and mass characteristics;
- Activation flags for models of the forces acting on the probe, together with all dynamic parameters involved^{†††},
- Earth stations locations,
- Initial and final times for trajectory together with probe’s initial conditions,
- Requested partial derivatives of solve-for parameters and of consider parameters (if existing).

PVDRIVE: integrates S/C trajectory and computes partial derivatives of state w.r.t. estimated/considered dynamic parameters;

TRANSLATE: translates instructions for data editing included in text files (*csp namelist*) to a *csp.nio* file to be used by subroutine *regres*. Editing includes:

- *Tracking data deletions*. Data are usually deleted for elevations lower than a certain value. For the present analysis lower limit of 20° have been set. Other cases of rejection include clear outliers, biased data, data received during maneuvers execution or during planetary occultation, or data belonging to passes exhibiting very large noise levels. Such data must be manually detected and deleted by user.
- *Data weighting*. Weights shall be assigned to the computed residuals to evaluate the cost function. Nominally weights are related to the noise level into

^{†††} For example, gravitational constant of celestial bodies for gravitational acceleration or optical coefficients of spacecraft components for solar radiation pressure.

the tracking data. Noise level is however dependent on the count time, therefore user set the expected noise level for data at a certain T_C (60 s), this value will be then corrected by the ODP by a factor equal to $\sqrt{60/T_{C_i}}$. In practice, weights are set such to match post-fit residuals *rms* value. A further weighting function is automatically applied by ODP which accounts for the minimum elevation encounter during the tracking, such that data tracked at low elevations are given a lower weight^{†††}.

- *Data correction*. Computed residual can be adjusted with additive terms to be applied to residuals, to compensate for troposphere and charged particles path delay. Spin compensation have been added by applying an additive term equal to $(1+240/221) \times f_{SPIN}$, until few months ago JPL provided tracking files which were already corrected for spin.

REGRES: Processes all tracking data performing light-time solution for each observation. Computes partial derivatives of observations w.r.t. requested parameters and constructs computed observables. Computes residuals at which applies the corrections supplied through TRANSLATE's *csp.nio* file.

SIGMA: Computes estimate vector that minimizes the weighted least squares of residuals between computed and observed observables. Compute estimate covariance. If required, maps solution and covariance. Namelist inputs include:

- Filter structure options (different kinds of filter and numerical implementations are available);
- Output format options;
- List of estimated parameters with their a-priori values and a-priori uncertainties (in form of a covariance matrix);
- List of consider parameters with their a-priori values and a-priori uncertainties (in form of a covariance matrix).

^{†††} Correction for elevation consists of multiplying the noise level set by the user with the following function: $E = 1 + 18/(ELV_{MIN} + 1)^2$. Rationale for this is that troposphere delay can be compensated only approximately, it is therefore preferable to downweight data which travels longer across the Earth's atmosphere.

GINUPDTF: updates the *gin.nio* (therefore our model of the universe) according to the latest solution (*sol.nio*) obtained by sigma program, rather than using a user defined namelist. It is used after the first iteration of the estimation loop.

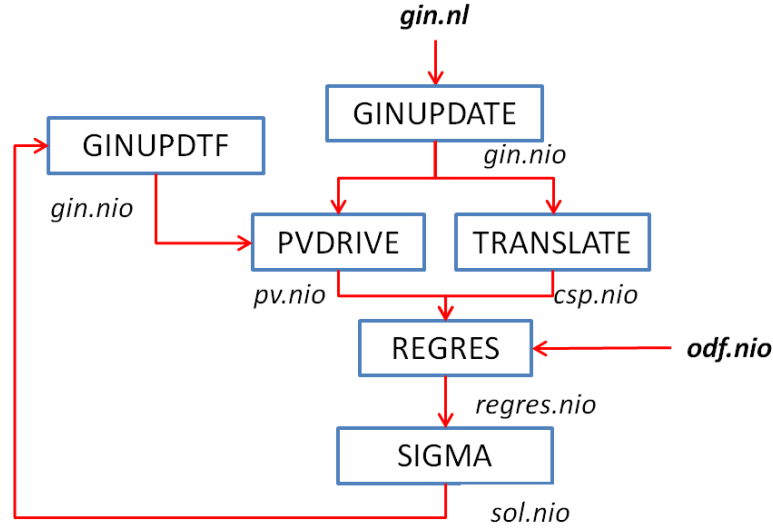


Figure 13: Schematics of the orbit determination process through ODP subroutines.

4.3 Criteria for estimate check

Estimation performed by ODP is an iterative process, this means that it should be stopped when it reaches convergence, which needs to be defined in practice. The main indicator for convergence is the Sum of Squares (SOS), defined as:

$$SOS = \sum_{i=1}^N \frac{(O_i - C_i)^2}{\sigma_i} \quad (6-2)$$

Where O_i represents the i -th measurement (*observed observable*), C_i is the i -th measurement reconstructed by *REGRES* (*computed observable*) and σ_i is the weight assigned via *csp* namelist.

ODP actually computes two kinds of SOS, the so called *pre-fit* and *post-fit* SOS. Pre-fit SOS is computed using residuals from *REGRES*. Post-fit SOS is computed after application of a differential correction to the residuals, using the solution computed by *SIGMA* and the partial derivatives of the computed observables with respect to solve-for^{§§§}. Due to non-linearity of the observables computation, pre-fit SOS at iteration k is different from the post-fit SOS of the $k-1$ iteration. As a consequence, residuals

^{§§§} These partial derivatives are an intermediate output of the orbit determination process computed by *REGRES*.

associated with the solution obtained by *SIGMA* at convergence, are the ones computed by *REGRES* at a successive iteration which is usually called *pass-through* (and which ends at *REGRES* level).

A common practice to avoid data overweighting is seek for a sum of squares slightly lower than the number of measurements, that is: $SOS \leq N$. Since the solution vector and the post-fit residuals depends on the weights assigned as input, and the weights should in turn verify eq. (6-2), that is, matching of residuals *rms*, weight assignment is an iterative process as well. It can be thought as a loop external to the estimation loop depicted in figure Figure 13.

As a rule of thumb, convergence is reached when the three following conditions are verified:

- post-fit SOS of the last two steps are similar;
- pre-fit and post-fit SOS of the same iteration step are similar;
- last post-fit SOS is slightly lower than N .

Other than checking convergence of the estimate, one should also check consistency and this is done by inspection of residuals and of the so called *Solution Summary*, a table which collects relevant output from *SIGMA*. Inspection of residuals have been already mentioned in section 4.1.3. As for the solution summary, it includes the following information for each solve-for parameter:

- *a-priori value* (starting value for the parameter as set by the user);
- *a-priori sigma* (square root of the *i-th* diagonal element of the a-priori covariance matrix);
- *corrected nominal* (estimated value at current step);
- *delta solution* (corrected nominal minus a-priori value);
- *terminal solution* (difference between corrected nominal at current step and corrected nominal at previous step);
- *a-priori solution* (delta solution changed of sign);

Based on this information, a certain parameter is said to be observable if its consider sigma is sensibly smaller than both the a-priori sigma and the corrected nominal: the first requirement indicates that the observations processed, brought actually information to improve the a-priori knowledge of a certain parameter; second requirement

guarantees that the estimated value is statistically significant and different from zero^{****}. Moreover, terminal solution shall not be greater than the a-priori sigma: this would be an indication that the a-priori sigma constrained excessively the estimate^{†††}. In such a case one would run again the filter increasing the a-priori sigma of the said parameter to then check if the new solution differs significantly from the previous and/or lead to a better fit of the data.

4.4 The tracking data

The tracking data made available by JPL have been collected by the Deep Space Network (DSN), a network of ground stations grouped in three complexes, at Goldstone, California, at Robledo de Chavela, near Madrid, Spain, and at Tidbinbilla, outside Canberra, Australia.

Communications between a spacecraft and the Earth are made within allocated frequency bands (Table 4).

Band	Uplink Frequency (MHz)	Downlink Frequency (MHz)
S	2110-2120	2290-2300
X	7145-7190	8400-8450
Ka	34200-34700	31800-32300

Table 4: Uplink and down link frequencies of DSN.

During this study, two-way and three-way Doppler data from Pioneer 10 and 11 have been analyzed. Loosely speaking a Doppler measurement is given by the comparison of transmitted frequency (from ground station or spacecraft) with received frequency on ground; frequencies are exclusively at S-band.

^{****} Under a certain set of hypotheses, the filter implemented by ODP provide a statistical representation of an estimated parameter as a randomly distributed Gaussian variable whose expected values is given by the corrected nominal, and standard deviation by the consider sigma. This means that the “real” value of the parameter has 99.7% possibility to lie within $\pm 3\sigma$ around its expected value.

^{†††} The cost function minimized by *SIGMA* includes besides the sum of the weighted norm of vector of measurement residuals vector, also the weighted norm of the a-priori residuals vector. This last is weighted with the inverse of the a-priori covariance matrix. If a priori covariance is set too small, departures from a-priori values are highly penalized hence constraining the estimate.

The frequency shift is proportional to the range rate w.r.t. the tracking station (*topocentric*, or *slant*), that is, the time derivative of the overall optical path in both directions (or the round trip light time):

$$\Delta\nu = \nu_0 \frac{1}{c} \frac{\Delta l}{\Delta t} \quad (0-3)$$

The optical path includes not only the geometric distance between the spacecraft and the tracking stations, but also several other effects such as relativistic light time delay, corrections due to interaction with media, and others. The detailed description of such effects is not of interest here and can be found e. g. in (Moyer, 2000). Actually the measurement performed at DSN is a sort of average frequency in terms of digitally counted cycles number per unit time. The frequency is averaged over a certain count time, T_C , therefore the Doppler records are the phase difference between the transmitted and received S-band frequencies, divided by T_C . As such, the observable is proportional to the change in optical path over of the count interval. The usual integration times for the Pioneer Doppler signals refers to the data sampled over intervals of 60 s, 600 s or 1980 s. A precise cycles count requires transmitted and received frequencies being coherent. The most accurate ranging and Doppler measurements are obtained via a two-way tracking mode for which the transmitting and receiving stations, and hence the frequency standards, are the same. For some missions, this configuration is impossible due to the huge distances: in such geometries, the transmitting station can rotate out of sight of the spacecraft by the time the signal returns to Earth, and thus, a second station is required. This is indeed the case for the deep space parts of Pioneers trajectories.

The information content of Doppler data does not directly allow retrieving of the position and velocity of the spacecraft in space. In fact, from geometrical considerations it can be shown (Thornton & Border, n.d.) that the Doppler signal sent by a deep space probe is essentially given by a ramp (representing the *geocentric* range rate) modulated by a sinusoid whose amplitude and phase depend on the declination and right ascension angles respectively. The sinusoid is the result of the tracking station rotation about Earth's spin axis. A single tracking of a spacecraft hence provides a measure of spacecraft radial velocity, right ascension, and declination. Velocity normal to the line of sight and range can be inferred from several days of Doppler data since the dynamics of spacecraft motion is constrained by Solar System gravitational (and non gravitational) force models, making spacecraft position and velocity fully determined.

This inference requires however a very accurate modeling of measurements and spacecraft dynamics, as summarized in paragraph 4.1.

Data analyzed during this study belongs to three orbit determination file provided by JPL:

- Pioneer 10 data after Jupiter encounter, spanning from 1979 to 2002.
- Pioneer 11 data during the rout from Jupiter to Saturn (fly-bys excluded), in the period 1977-1979.
- Pioneer 11 data after Saturn encounter, from 1980 to 1990.

4.5 Filtering techniques for orbit analysis

As far as the implementation of the ODP analyses is concerned, two different techniques have been applied, which are discussed below.

4.5.1 *Single-arc analysis*

In a single-arc analysis all the data are processed at once, using as estimated parameters the initial state of the spacecraft, and maneuvers magnitudes. These were modeled with instantaneous velocity increments. Addition of exponentially decaying accelerations used to compensate for possible gas leaks after maneuvers has also been evaluated; both velocity increments and exponential accelerations have been treated as solve-for parameters.

In order to compensate for modeling inaccuracies, (of which the Pioneer Anomaly is surely an indicator by itself) an additional capability of *SIGMA* can be exploited which includes the use of stochastic dynamical processes. This is part of the Kalman batch-sequential Filter-Smoother implementation of the estimator. In this approach, every small force which cannot be included and/or estimated in a deterministic manner, is treated as a stochastic parameter which affects spacecraft trajectory. These processes are specified by a set of stochastic attributes^{****}:

- *Model_P*, specifies the kind of stochastic process used to model the parameter, *colored* and *random walk* noises are available.

^{****} They will be named following the syntax of the program.

- Tau_P , a characteristic time which represents the correlation time for colored noise (white noise if it is set to 0); for random walk, it is the time by which standard deviation increases by $Sigma_P$.
- $Sigma_P$, which is the steady state standard deviation for colored noise; for the random walk model it is the increase in standard deviation in a time Tau_P .
- $Delta_P$, the time interval (batches) between updates of the stochastic parameter. The parameter can be chosen to be constant within the batch, or to follow a cubic spline variation.

In the case of Pioneer spacecrafts, one may then think at the anomalous acceleration as the sum of a constant bias plus a stochastic process. This strategy has been used in (J.D. Anderson, Laing, et al., 2002) to check for possible time variations of the anomaly^{§§§§}. Introduction of such compensation techniques may however be quite “dangerous”, in the sense that these are phenomenological accelerations which do not rely on physical basis. Moreover, the stochastic processes may adsorb not only model errors (i.e. the *process noise*, in Kalman Filter like nomenclature), but also observational noise leading to a fictitious increase in the quality of data fitting. Finally, the use of additional accelerations may introduce a bias in the estimate of the “real” anomalous acceleration.

4.5.2 Multi-arc analysis

In principle the trajectory followed by a spacecraft, no matters how long in time it is, can always be fitted by a single orbit which is dependent on a set of initial conditions. It is reasonable therefore to include all the tracking data available for a certain spacecraft into a single analysis, so that all of the observables contributes to the estimate. On the other hand, the complexity of the physics underlying spacecraft dynamics makes it highly improbable that it can be perfectly represented by a single deterministic model, so that, in practice, one must deal with a certain degree of model deficiency. From the point of view of the estimate, one can say that there are parameters which cannot be

^{§§§§} Stochastic processes are inherently time varying. On contrary, WLSQ filter representation of time varying accelerations is limited to a small set of deterministic functions of time (exponential, polynomials).

accurately included nor estimated within the filter: the effect which such parameters have on spacecraft dynamics is small (that is why they cannot be estimated) but accumulates in time so that, for sufficiently long time span, modeling errors grow beyond observational errors deteriorating the estimate.

Pioneers tracking data, lasting more than a decade, are likely to be prone to such a problem. To overcome these difficulties multi-arc analysis, which has been recently used for Cassini spacecraft navigation (Di Benedetto, M. Iess, L. Roth, 2009), can be used. With this method, orbital fits are obtained from shorter data arcs (from 6 months to 1 year in the present study). In the multi-arc technique the set of estimated parameters is separated into two groups: global parameters common to all arcs, and local ones which are affected only by the single arc to which they refer to (see appendix A), and are introduced to adsorb not adequately modeled dynamics (Di Benedetto, M. Iess, L. Roth, 2009). The possibility of modeling errors for Pioneers trajectories has emerged in previous works: in (Levy et al., 2009), spectral analysis of post-fit residuals highlighted periodic terms at half a sidereal day, one sidereal day and half a year. In (J.D. Anderson, Laing, et al., 2002) an annual oscillatory term in a stochastic acceleration model have been found.

For Pioneers probes, parameters which may be treated as local, other than initial state vector, are the maneuvers velocity increments; the anomalous acceleration is set as global parameter.

Implementation of multi-arc within ODP

Multi-arc simulations can be practically achieved with the ODP by using fictitious multiple spacecrafts, each of them “travelling” on a segment of the complete trajectory. For each spacecraft, the orbit determination steps shown in the schematics of Figure 13 are performed up to *REGRES*. These steps are performed in parallel since the ODP runs on multi-core pc. Each spacecraft, which is identified by a number, has its own *gin* namelist where initial and final time of trajectory arc, plus state vector at epoch are set: the ODP treats each batch of data as if it was generated by different spacecrafts, which in our case are the same (same geometry and mass). As for single spacecraft, a list of partials for the desired solve-for or consider parameters is written. This time, however for the parameters to be treated as local, an identifier is appended to their standard name constituted by a # followed by the spacecraft number. In principle there can also be

different tracking data file (*odf.nio*); this is not the case for Pioneer 10 which has one single tracking file and for each spacecraft only the tracking data between the initial and final times will be used by *REGRES*. After *regres.nio* files have been generated for each spacecraft, these are merged in a single file using one dedicated ODP subroutine called *ODMERGE*. Estimation filter is then run through *SIGMA*: the main difference with the single-arc implementation is that now the parameters treated as local are affected only by the observation of the single arc: to be a bit more specific, the partial derivatives of the computed observables with respect to observations are non-null only for the observations of that specific arc. On contrary, global parameters appear in the partial derivatives of all the observations. In other words, initial conditions of a certain arc, which are local parameters, are not constrained by other arcs. The same happens, for example, for the maneuvers occurring during that arc. The anomalous acceleration acting on the probes, has instead been treated as a global parameter so that all of the available data contribute to its estimate.

A schematics of the multi-spacecraft run mode of the ODP is depicted in figureFigure 14. In this figure it is also included the iteration loop for weights assignment which has been implemented^{*****}. This consists of two routines, the first extracts relevant information from *regres* file: the value of residuals (prior and after corrections), the identifiers of uplink and downlink stations, the time-tag, count time, and the kind of Doppler data (two-way or three-way). The second, basing on these information, clusters the residuals in groups of homogeneous data and for each of them computes the *rms* value, applies the conversion factor to normalize the weight at 60 s of count time, and write the *csp* namelist accordingly.

^{*****} Credits for most of the development of the automatic-weights routines goes to Ing. Marco Zannoni and Ing. Gilles Mariotti of the Radioscience lab at Second Faculty of Engineering of University of Bologna.

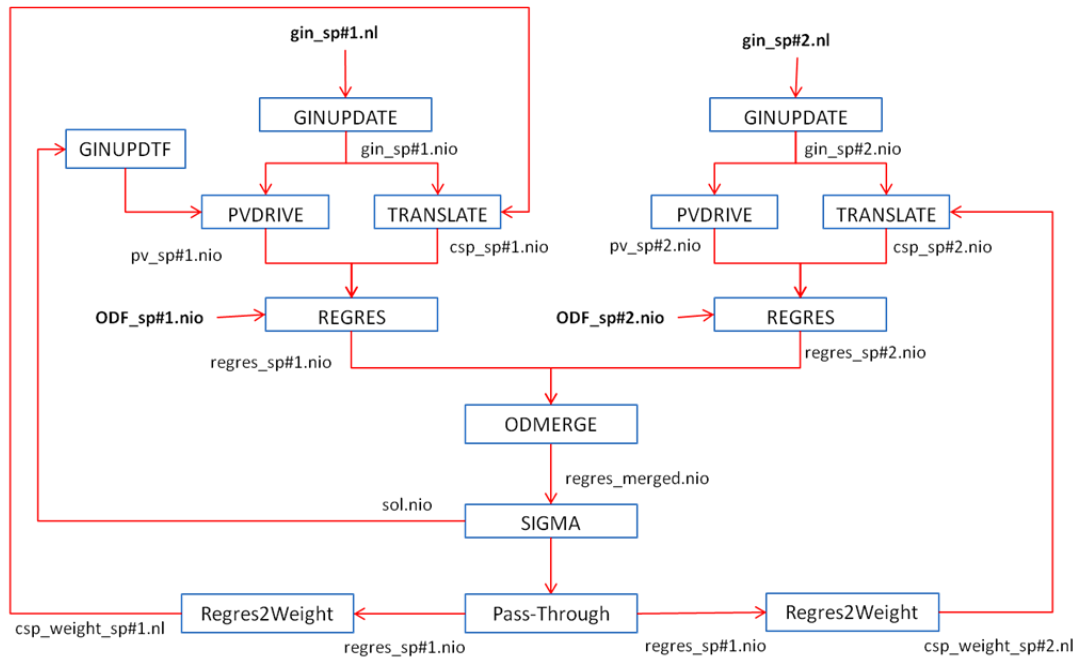


Figure 14: Schematics of the implementation of multi arc data analysis within ODP.

4.6 Data preparation and editing

Data editing capabilities offered by the ODP have been briefly discussed in section 4.2. For the analyses performed during this study, seasonal corrections for tropospheric dry and wet delay have been included, while the adoption of ionosphere path delay have been evaluated based on Klobuchar model (Klobuchar, 1975) but soon disregarded since did not provide a substantial improvement to the fitting. Spin compensation has been added using *csp* namelist to adjust residuals. However recently newly recovered tracking data were made available by JPL with spin calibration already included. To mitigate possible effects on the analysis due to solar plasma, data have been deleted during solar conjunctions, using a threshold value for SEP angle of 20° . Outliers and biased data has been deleted as well.

Doppler observables have been weighted with the standard deviation of the residuals computed subset of data, using an automatic iterative routine for weight assignment. In this fashion the post-fit SOS is slightly lower than the number of Doppler data which therefore are never over-weighted.

Results

5.1 Analysis on first set of data prior to thermal modeling

The most referenced solution for the Pioneer Anomaly (J.D. Anderson, Laing, et al., 2002) $a_p = (8.74 \pm 1.73) \times 10^{-10} \text{ km/s}^2$ has been obtained from a set of data from Pioneer 10 covering the period from 1987 to 1998^{†††††}. This is the set of data also available during the majority of the Ph.D. (extended data set of Pioneer 10 and Pioneer 11 data have been made available in late 2011). First attempts to retrieve the value of the constant anomalous acceleration (therefore without including thermal dissipation) were made at first and soon was clear that the result was dependent on the techniques used to model the 29 precession maneuvers occurred during the period. As said in section 4.1.1, in principle precession maneuvers should not directly act on spacecraft state vector, unless imperfect thruster operation gives rise to unbalanced forces.

Support to such occurrence in case of Pioneer 10 can be found by inspection of the Doppler data. Figure 15 shows the Doppler residuals in proximity of the maneuver performed on 1st June 1987. Two features are quite evident in the picture: first the presence of a gap between the two arcs of data, indicating a velocity jump across the maneuver. Secondly, the different slope of the two arcs, which suggests a variation in the magnitude of the unmodeled acceleration; this may have been caused by gas leaks occurring after the completion of the maneuver.

^{†††††} The extended data set 1979-2002 has been made available only more recently, and mostly of the published papers on this topic have relied on the “older” tracking file.

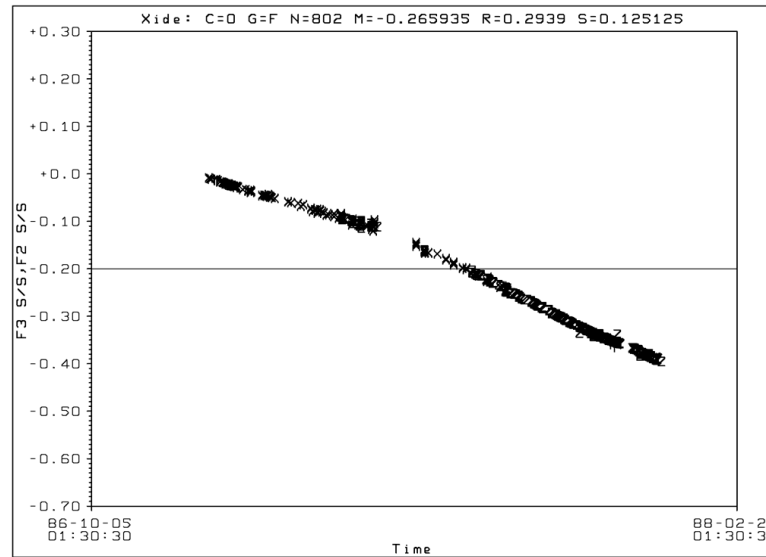


Figure 15. Doppler residuals (Hz) in proximity of June 1st 1987 maneuver.

Times at which maneuvers have been operated are available through telemetry, together with records of commanded thrusters pulses. From this data, however, it is not possible to infer the magnitude of the (unintended) velocity increments possibly occurred during maneuvers. Rather, the only means of estimating such velocity increments is using the radio-metric data, that is, to treat them as solve-for in the orbit determination analysis and check if such parameters are actually observable and/or improve the quality of the fitting. This has been the case for all of the precession maneuvers occurred during the time span covered by the tracking data analyzed.

ODP offers several models to describe maneuvers, most relevant are:

- Finite burns model;
- Instantaneous burns model;
- Quadratic gas leaks;
- Exponential gas leaks;

The latter two account for accelerations ($\ddot{\vec{r}}$) which may rise after the nominal end of the propulsion due to jet leakage, implemented as a quadratic polynomial of time, or decaying exponential. Finite burn and instantaneous burn models implement velocity increments ($\Delta\vec{v}$) generated by gas firings, but while the first specifies the propulsive force as a 4th order polynomial of time within a finite interval, the second assigns discrete velocity jumps at a certain time instant. Since precession maneuvers duration is usually quite short (length on the order of a hour), it has been chosen to model them as instantaneous burns. During the investigation it has been further checked whether only

Results

the line of sight (Z in spacecraft axis) component could be observed, as should be expected from Doppler data, or if also out of sight components may be observed.

As for the presence of gas leaks, this is a delicate question since their estimate may highly correlate with the anomalous acceleration: a constant acceleration may be mimicked by a series of propulsive accelerations which act all on the same direction. If thrusters malfunctioning may have happened, it is highly unlikely that the effect would have generated accelerations always in the same direction, and for both spacecrafts. Moreover, as reported in (Slava G. Turyshev & Toth, 2008), telemetry data give no indication of a loss of fuel. In general one can say that gas leaks, if occurred, could not have been responsible for the entire anomaly, but might nevertheless have affected its estimated value. It has therefore been chosen to investigate this issue by activating several exponentially decaying acceleration models, in between each couple of subsequent instantaneous maneuvers. In particular for such model it holds (Jet Propulsion Laboratory Navigation Software Group, 1996):

$$\ddot{r} = (A_r \hat{Z} + A_x \hat{X} + A_y \hat{Y}) e^{-\beta \Delta t} \quad (7-1)$$

Where only the radial Z component of the acceleration, ^{****} A_r , has been set as solve-for since the others are made unobservable by the spin motion of the spacecraft ($A_x \equiv A_y = 0$). The time constant for the decay, $1/\beta$, has been set as a fixed input common for all leaks (not estimated) and two values have been tested: $1/\beta \approx 10$ or 60 days.

The following test cases have been performed, for which the solve-for parameters have been set as:

1. Line of sight ΔV ;
2. Line of sight ΔV plus exponential gas leaks magnitude;
3. Three components ΔV ;
4. Three-components ΔV plus exponential gas leaks magnitude;
5. Three-components ΔV plus stochastic acceleration as colored noise.
6. Multi-arc (three-components ΔV + three-components Δr).

For all cases a constant acceleration, the anomaly, has also been treated as solve-for. As for test case 5, which includes a stochastic parameter, it is one sample taken between several tests performed to investigate the effect of changes in correlation time and update time (length of batch).

^{****} In eq.(6-1) The X-Y-Z axes are spacecraft axis and Z coincides with spin direction.

Results

Other parameters, are treated as consider parameters and their uncertainty accounted for. These include, the Solar Corona parameters, tropospheric dry and wet zenith delay corrections, Earth stations locations, and the antenna reflectivity coefficients (see Table 6).

For the multi-arc filter, the a-priori state vector components at the beginning of each arc were generated by mapping the orbital solution obtained on a single arc to the epochs of interest. As for the a-priori sigma, there are two opposite requirements: on one hand one would allow for high a-priori sigma since the initial conditions of the arc is a local parameter independent from other arcs; on the other hand, we know that the arcs belong to the same trajectory and it would be unphysical if the estimate ends to a set of arcs which are completely disconnected in space. Taking these considerations into account it has been set:

- a-priori sigma of position vector equal to the mapped covariance from single arc solution multiplied by a magnification factor (values of 5 and 10 have been tested);
- a priori sigma of velocity components have been set independently from mapped ones, and set to 0.1 m/s to allow for correct estimate of maneuvers ΔV .

In this way each arc's state vector at epoch is practically independent from the others, yet the reconstructed trajectory is not highly discontinuous.

The separation time for the arcs are the maneuvers for two reasons: firstly in this way there is a certain similarity with the single-arc approach, since both allow for discontinuities at maneuvers (the former allows for velocity jumps, while multi-arc allows for both velocity and position jumps). Secondly, maneuvers were performed approximately every six months, which is the time scale at which periodic signatures have been detected in the residuals, indicating that this is a time scale at which model deficiencies rise up.

Results are found in Table 5 where post-fit residuals mean, standard deviation and plot, and estimated acceleration with formal accuracy (accuracy in presence of consider parameters is reported between round brackets) are displayed in Table 4.

Firstly we focus on the quality of the fit: what emerges is that a single ΔV component clearly provides an inadequate description of spacecraft dynamics which leads to a poor fitting quality with evident deterministic signatures in the residuals. Out

of sight components increase sensibly the quality of the fitting; if one looks at the consider sigma of the solution parameters, it appears that for several maneuvers ΔV_X and ΔV_Y are actually observable parameters (consider sigma 5 to 10 times smaller of corrected nominal). Adding exponential gas leaks slightly improve the quality of the fitting (i.e. lower residuals *rms*) with a greater benefit when using the higher time constant. Test case 5 includes an acceleration modeled as a colored noise with $\sigma = 5 \times 10^{-13}$ km/s²., update time of 1 day and correlation time of 12 hours. Multi arc gives a very good fit underperforming only slightly the stochastic filter.

When looking at the estimated constant acceleration, the estimated value is clearly dependent from the strategy used to model maneuvers, as expected. The biggest variations occur when adding gas leaks. A bit surprisingly, one can see that the residual acceleration increases when adding leakage: the possibility that part of the anomaly may be fictitiously adsorbed by a series of exponential acceleration all having the same sign did not occur, and, actually, estimated leaks have different signs. Consider sigma of the estimate increase also when adding exponential gas leaks, because of the increase number of solve-for parameters. This is even more evident with multi-arc which requires the highest number of solve-for. Estimated acceleration using multi-arc results in a lower value indicating that probably a part of the bias estimated from a single arc is caused by other sources of modeling errors. This consideration is also supported by the result of stochastic filter. It is interest to note that noise compensation via stochastic (# 5) or deterministic (# 6) strategies lead to estimated accelerations which are statistically equivalent within 2- σ bounds.

5.1.1 Comparison with other published solutions

Comparing with other published analyses of the same Pioneer 10 data set can be twofold, on one side comparing residuals standard deviation, on the other side estimated anomalous acceleration.

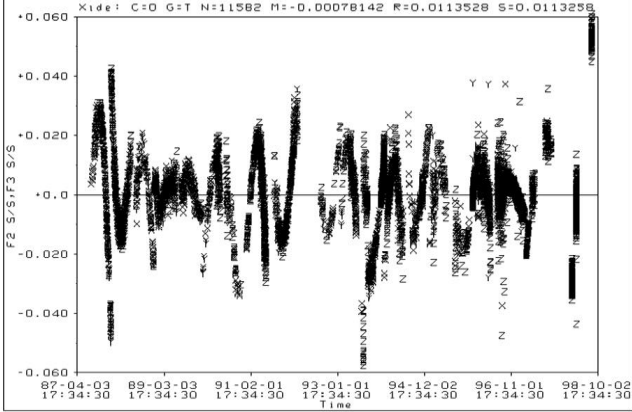
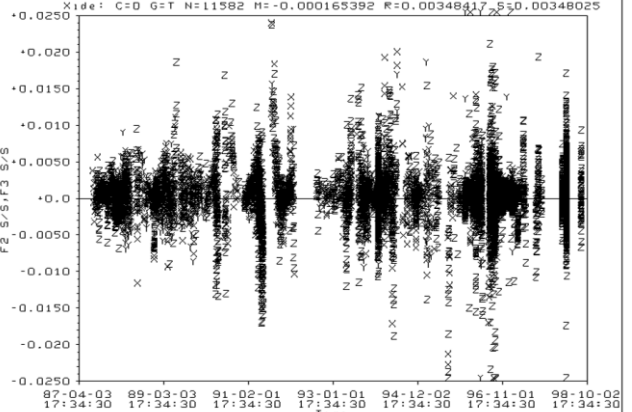
For comparing the results obtained in terms of estimated acceleration with previous works, the most appropriate reference seems (J.D. Anderson, Laing, et al., 2002) where an orbit determination through *SIGMA* has been performed on the same set of Pioneer 10 data; In that reference, the 11 year long arc has been split in three batches and gas leak following the burn were modeled by fitting to the post-maneuver residuals an exponentially decaying model for ΔV , with time constant treated as solve for, and

Results

reported to be 13 days for a sample maneuver. Results, prior of accounting for all systematics, led to (see table 1 in the reference) the estimations: 8.02 ± 0.01 , 8.65 ± 0.01 and 7.83 ± 0.01 for the three batches. When compared to test cases 2 and 3 (the most similar in terms of filter set-up) results are in close agreement. Residuals quality can be compared against the *rms* value of ≈ 3 mHz obtained from the orbit solutions presented in this section (see Table 5). In (J.D. Anderson, Laing, et al., 2002) no precise information on *rms* value are found but the residuals depicted in figure 13 indicates that the obtained solutions are at least comparable with the reported one. Other references, such as (Levy et al., 2009; Craig B. Markwardt, 2002), show pictures of residuals from this same batch of data; (Levy et al., 2009) also reports residual standard deviation to lie between 9.8 and 5.5 mHz. These results however are achieved with different OD software and the comparison is less significant.

Conclusions from these tests can be summarized as follow: even if the tracking data themselves cannot tells us for sure that fuel leaks occurred, what we can say is that over-parametrization performs as expected, that is, increases the quality of the fitting. In principle, gas leaks can be considered similarly to as the application of multi-arc filter since they introduce additional solve-for parameters. The reduction of residuals *rms* comes however at the expense of a loss of formal accuracy (increase in consider-sigma) which is a well known effect in LSQ filters when augmenting the number of estimated parameters without adding information from observations. Same holds for process noise compensation with the stochastic filter-smoother. Tests using leakage and stochastic acceleration models give also an important indication, that is, *one single constant* acceleration does *not* provide the best fitting of the data, unless multi-arc is performed. On the other hand, they provide a sensibly different estimated value of the anomalous acceleration which is less significant since now it is just *one part* of the total estimated acceleration (constant bias plus a series of other short term accelerations).

Results

Test case	Post-fit residuals μ, σ [mHz]	Estimated acceleration [Km/s ² ×10 ¹³]	Plot of residuals
1	$\mu = -0.78$ $\sigma = 11.3$	7.253 ± 0.022 (0.025)	
2	$\mu = -0.17$ $\sigma = 3.5$	7.908 ± 0.020 (0.027)	

Results

3	$\mu = -0.07$ $\sigma = 3.2$	8.241 ± 0.027 (0.034)	
4	$\mu = -0.04$ $\sigma = 3.1$	9.253 ± 0.068 (0.085)	

Results

5	$\mu = -0.04$ $\sigma = 2.8$	$7.31 \pm 0.05 (0.14)$	
6	$\mu = -0.07$ $\sigma = 3.0$	$7.51 \pm 0.10 (0.15)$	

Table 5: Summary of preliminary analysis of Pioneer 10 first set of radiometric data (1987-98).

Parameter	A-priori Sigma
MUF ^{§§§§§}	0.04
NUF	0.1
CORONA	4×10^3
CORONB	1.8×10^2
CORONC	0.8×10^6
TROPWj (j=1,2,3)	5×10^{-5} m
TROPDj (j=1,2,3)	1×10^{-4} m
LOii	1.57×10^{-5}
CUii	1×10^{-4} m
CVii	1×10^{-4} m

Table 6: Parameters treated as consider with relative covariance (nomenclature follows ODP syntax, see footnote for explanations).

5.2 Orbit analysis of Pioneer 10 and 11 complete set of data in light of thermal model.

Our efforts in performing the analyses using ODP were aimed at obtaining satisfactory orbital solutions incorporating the TRA, besides the above mentioned built-in dynamical models, possibly without adding any other residual, unexplained acceleration. Even if the computed TRA depicted in Figure 11 are time varying in contrast with the constant acceleration reported in (J.D. Anderson, Laing, et al., 2002) or decreasing monotonically (S.G. Turyshev et al., 2011), one should keep in mind that the measured anomaly is actually a Doppler shift in the radio-metric data, while the reported solutions for accelerations are just one way to obtain good orbital solution (i.e. fitting of tracking data). Other orbital solutions may be sought based on dynamical models which differ from one single acceleration, and possibly relying on a physical basis. In fact, the thermal analysis presented above provides one such model.

^{§§§§§} MUF NUF = μ_F, ν_F coefficients of HGA Earth pointing side; LOii, CVi, CUii = Longitude (*deg*), height above equator (*km*) and spin axis distance (*km*) of Earth Station *ii*; CORONA, CORONB, CORONC = characteristics constant for solar corona path delay; TROPDj, TROPWj = constant corrections to tropospheric zenith dry and wet path delay at DSN Complex *j*

Results

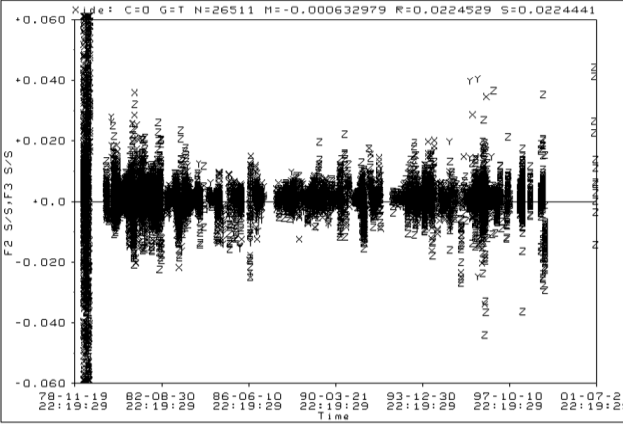
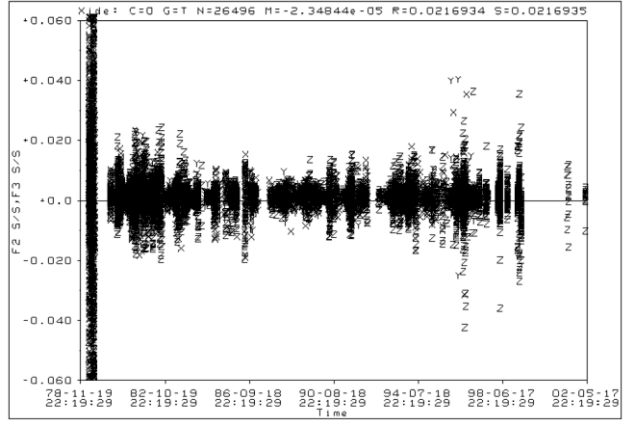
The first analysis performed consisted in re-estimating a constant anomalous acceleration using the extended data set of Pioneer 10 and 11, without accounting for the output of the thermal analysis using both single-arc and multi-arc filtering. This first test group is identified with the number 0, followed by an indicator of the spacecraft (P10 or P11) and of the filter (SA, MA). For Pioneer 11 there are two well separated trajectory segments, the first encompassing the Jupiter to Saturn transfer orbit and denoted with “preS”, and a longer data set one for post Saturn encounter trajectory (“postS”). These have been treated as separated batches, then as combination of two arcs (labeled with 2A to indicate a multi-arc with only 2 arcs) but also as a set of multiple arcs each lasting approximately one year.

In light of the discussion in section 5.1, the use of gas leaks or dynamic compensation with stochastic accelerations has been definitely abandoned in favor of multi-arc filter to avoid biasing the acceleration estimate. An additional reason to prefer deterministic dynamic compensation with respect to stochastic one is that the latter requires search of an optimum combination of correlation time, update time and sigma level, which is something completely empirical. As a consequence, each maneuver has been modeled with three solve-for parameters, the instantaneous velocity increments along three axes.

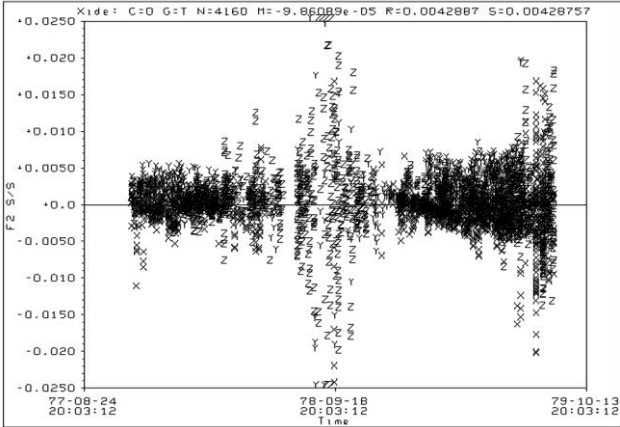
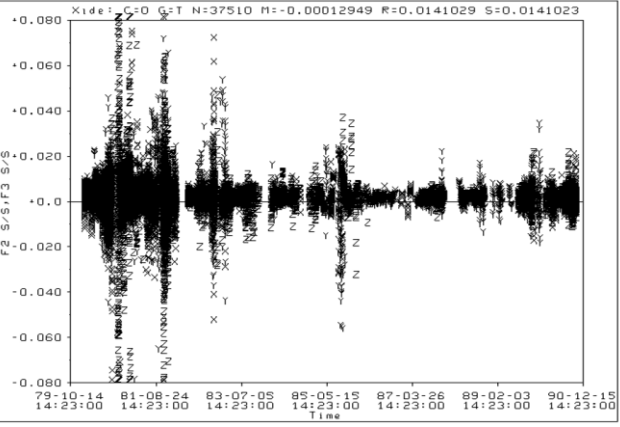
As for multi-arc filter, for Pioneer 10, a total of 46 arcs were implemented, one at each maneuver occurrence, lasting approximately 6 months each. For Pioneer 11, due to the very large number of maneuvers, it would have been unpractical to create one arc between each couple of maneuvers; moreover, it should be remembered that the dynamic compensation has been motivated mainly by the evidence of half a year periodic signatures in residuals (Levy et al., 2009) and annual oscillatory term in the acceleration (J.D. Anderson, Laing, et al., 2002), which indicates the time scale at which modeling errors become significant. We used a total of 11 arcs lasting approximately one year, each having a number of maneuvers treated as local solve-for parameters. As done for the preliminary study discussed in section 5.1, the a-priori initial conditions have been retrieved from single arc solutions, with a-priori sigma softly constraints only on position components, letting velocity components free to compensate for precession maneuvers.

The different orbit solutions obtained are compared in terms of the mean (μ) and root mean square (σ) values of the residuals. Results are summarized in Table 7.

Results

Test case	Post-fit residuals μ, σ [mHz]	Estimated acceleration [Km/s ² × 10 ¹³]	Plot of residuals
0.P10/SA	$\mu = 0.63$ $\sigma = 22.4$	8.051 ± 0.019	
0.P10/MA	$\mu = -0.03$ $\sigma = 21.4$	7.96 ± 0.17	

Results

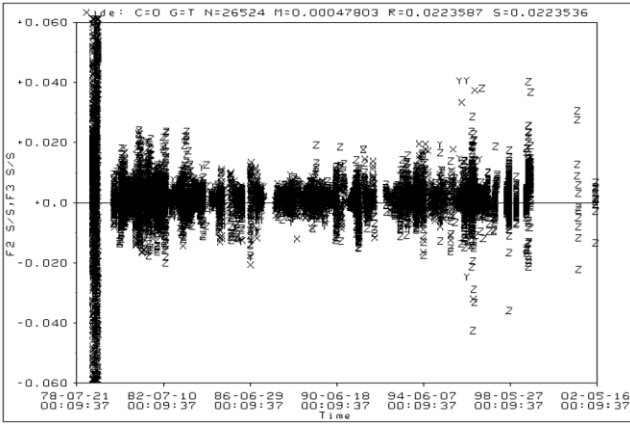
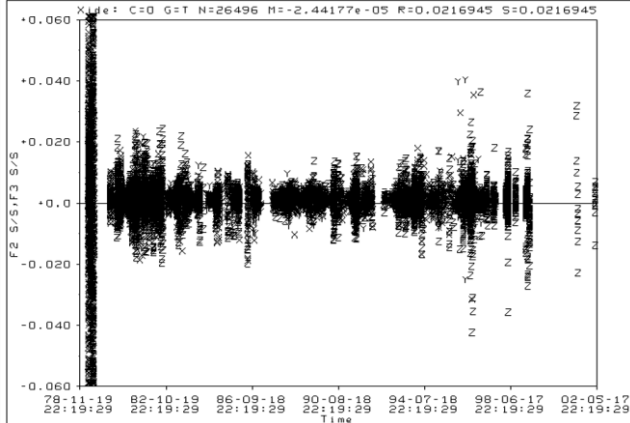
<p>0.P11- preS/SA</p>	<p>$\mu = -0.1$ $\sigma = 4.3$</p>	<p>0.24 ± 0.50</p>	
<p>0.P11- postS/SA</p>	<p>$\mu = -0.13$ $\sigma = 14.2$</p>	<p>8.96 ± 0.25</p>	

Results

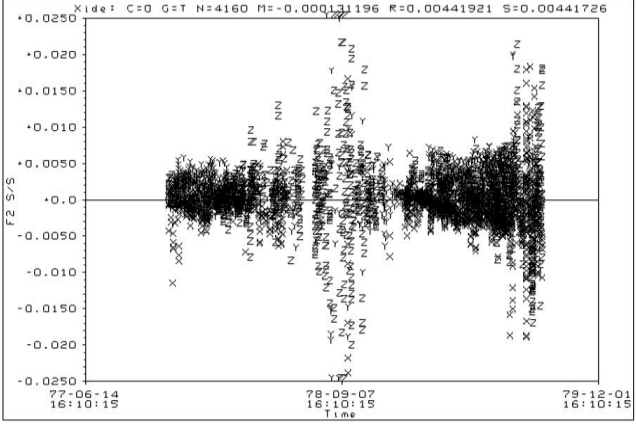
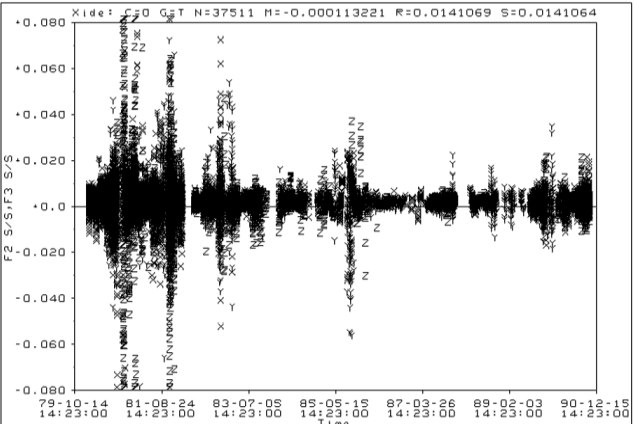
<p>0.P11/2A</p>	<p>$\mu = -0.12$ $\sigma = 13.4$</p>	<p>7.25 ± 0.27</p>	
<p>0.P11/MA</p>	<p>$\mu = -0.10$ $\sigma = 13.5$</p>	<p>6.93 ± 0.17</p>	

Table 7: Summary of Test Set 0 of orbit analyses of Pioneer 10 and 11 with estimation of anomalous acceleration.

Results

Test case	Post-fit residuals μ, σ [mHz]	Plot of residuals
1.P10/SA	$\mu = -0.09$ $\sigma = 22.3$	 <p>Residual plot for 1.P10/SA. The y-axis is labeled 'F2 S/S/F3 S/S' and ranges from -0.060 to +0.060. The x-axis is labeled 'Time' and shows dates from 78-07-21 to 02-09-19. The plot shows a dense distribution of residuals around zero, with a slight negative bias. Statistics: X=0, Y=0, N=26524, H=0.00047803, R=0.0223587, S=0.0223536.</p>
1.P10/MA	$\mu = -0.02$ $\sigma = 21.7$	 <p>Residual plot for 1.P10/MA. The y-axis is labeled 'F2 S/S/F3 S/S' and ranges from -0.060 to +0.060. The x-axis is labeled 'Time' and shows dates from 79-11-19 to 02-11-19. The plot shows a dense distribution of residuals around zero, with a slight negative bias. Statistics: X=0, Y=0, N=26496, H=-2.44177e-05, R=0.0216945, S=0.0216945.</p>

Results

<p>1.P11- preS/SA</p>	<p>$\mu = -0.13$ $\sigma = 4.4$</p>	 <p>Xide: C=0 G=T N=4160 M=-0.000131196 R=0.00441921 S=0.00441726</p> <p>77-06-14 16:10:15 78-09-07 16:10:15 79-12-01 16:10:15</p>
<p>1.P11- postS/SA</p>	<p>$\mu = -0.11$ $\sigma = 14.1$</p>	 <p>Xide: C=0 G=T N=37511 M=-0.000113221 R=0.0141069 S=0.0141064</p> <p>79-10-14 14:23:00 81-08-24 14:23:00 83-07-05 14:23:00 85-05-15 14:23:00 87-03-26 14:23:00 89-02-03 14:23:00 80-12-15 14:23:00</p>

Results

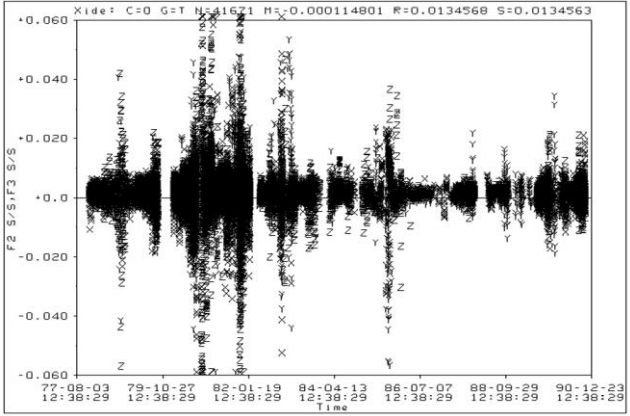
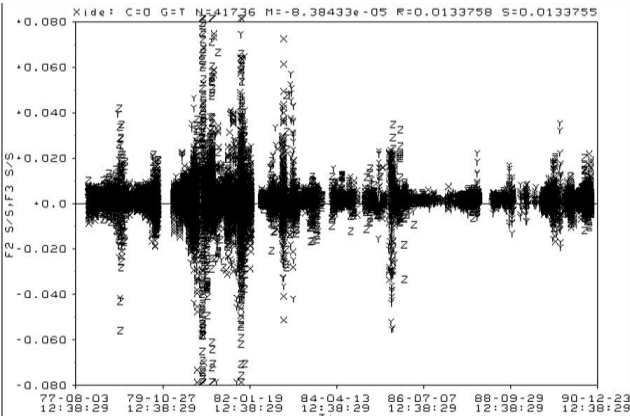
<p>1.P11/2A</p>	<p>$\mu = -0.11$ $\sigma = 13.5$</p>	
<p>1.P11/MA</p>	<p>$\mu = -0.08$ $\sigma = 13.3$</p>	

Table 8: Summary of Test Set 1 of orbit analyses of Pioneer 10 and 11 with thermal recoil acceleration included as dynamical model.

Results

Test case	Post-fit residuals μ, σ [mHz]	Estimated acceleration [Km/s ² × 10 ¹³]	Plot of residuals
2.P10/SA	$\mu = 0.63$ $\sigma = 22.4$	0.21 ± 0.43	
2.P10/MA	$\mu = -0.018$ $\sigma = 21.8$	0.88 ± 0.55	

Results

<p>2.P11- preS/SA</p>	<p>$\mu = -0.12$ $\sigma = 4.3$</p>	<p>0.70 ± 0.73</p>	
<p>2.P11- postS/SA</p>	<p>$\mu = -0.13$ $\sigma = 14.2$</p>	<p>-1.35 ± 0.81</p>	

Results

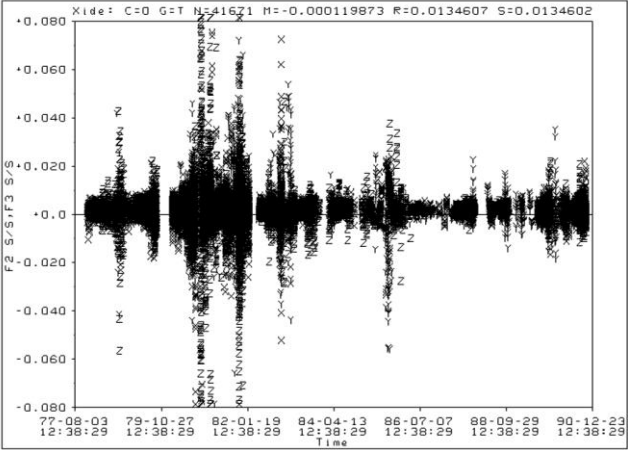
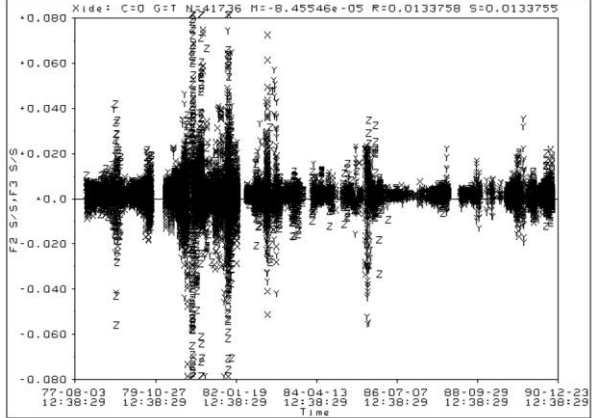
2.P11/2A	$\mu = -0.12$ $\sigma = 13.4$	-1.87 ± 0.7	
2.P11/MA	$\mu = -0.07$ $\sigma = 3.0$	-1.5 ± 0.47	

Table 9: Summary of Test Set 2 of orbit analyses of Pioneer 10 and 11 with thermal recoil acceleration included plus additional acceleration as solve for.

The values obtained from this preliminary test case are quite similar to those of other references. As for the earlier data of Pioneer 11 (transfer from Jupiter to Saturn) the value of the acceleration is statistically null, in accordance with what reported in (S.G. Turyshev et al., 2011). As a matter of fact, in this part of trajectory solar pressure is dominant with respect to the acceleration of thermal origin, which drops down to small magnitudes (see Figure 11). Moreover, a trajectory maneuver was performed on July 1978 of several meters per second along track which may hide the ΔV caused by any small acceleration. In general, tracking data of both segments of Pioneer 11 trajectory

Results

stays within heliocentric distances at which solar pressure is at least comparable to thermal recoil acceleration. In fact, if we add μ_F and ν_F as solve-for parameters, the resulting acceleration varies considerably. We set the a-priori uncertainty of the reflection coefficients equal to 20% of their magnitude and the estimated acceleration of cases 0.P11/2A drops down to 7.10 ± 0.19 . This is an indication that the actual magnitude of the anomalous acceleration is correlated to solar pressure, or equivalently, a portion of the anomalous acceleration may be due to errors in modeling of SRP. The analysis of the first segment of Pioneer 11 trajectory allows for some considerations on the onset of the anomaly. One would say that the anomaly appears only at post-Saturn distances; actually available data tells us than an acceleration of order of magnitude 10^{-12} km/s³ or less is simply hardly observable, this is clear by looking at the consider sigma of test case 0.P11-preS/SA. If we assume IR radiation being the cause of the anomalous acceleration, than our thermal model seems to correctly predict the trend of a decreasing acceleration between Saturn and Jupiter. This is however just a bit more than a speculation because of the uncertainty in estimation just mentioned.

Afterwards, this tests have been repeated with the following variants:

- Test Set 1, where the thermal recoil acceleration model is included in trajectory reconstruction and treated as consider.
- Test Set 2, where TRA is included as consider and an additional bias acceleration is retained as solve-for (global parameter in case of multi-arc).

The inclusion of an additional acceleration has the purpose of checking whether thermal recoil force is enough to explain the whole anomaly, or if a residual unmodeled acceleration still exists and provides a better orbital solution. For Test Set 2, additional parameters are treated as *consider*, which include the ones found in Table 6 plus the coefficients for the thermal recoil acceleration as found in Table 3.

Results are summarized in Table 8 and Table 9 and discussed hereafter.

When including time varying accelerations according to our thermal model, orbital solution are obtained for Pioneer 10 and for the two segments of Pioneer 11, without adding any other acceleration. This is an implicit confirmation that the observed drift in Doppler residuals is compatible with time varying acceleration. References (Craig B. Markwardt, 2002) and (S.G. Turyshev et al., 2011) showed this by adding monotonically decreasing accelerations as solve-for, we instead verify a posteriori such hypothesis by adding a new dynamic model (the computed time-varying thermal recoil

Results

acceleration) to the orbit determination process. Quality of the fit is comparable with solutions obtained with Test Set 0, in particular, no drift or signatures are evident which may indicate for residual anomalies. A confirmation of this is found with Test Set 2: the additional acceleration cannot be clearly estimated, since the estimated value is not sufficiently larger than its consider sigma. Even when the estimated value is larger than 2-sigma, there is no gain in the orbital solution quality by the introduction of a new acceleration.

All the above considerations hold for both Pioneer 10 and 11, as well as for single-arc and multi-arc filtering.

As a side note, it can be shown that the over-parametrization has a marginal beneficial effect on quality of the orbital solution when comparing the overall residuals *rms* value. However when excluding the highly noisy first part of the data corresponding to year 1979 for Pioneer 10, the improvement is more evident with residuals lowering from 3.7 down to 3.3 mHz.

In summary all the simulations performed goes in the same directions, that is, there is no anomalous acceleration acting on Pioneer 10 and 11. The repeatedly reported unexplained drift in Doppler residuals disappears when including the force due to anisotropic IR emission into the dynamical model of the probes.

Conclusions and recommendations

The work presented in this report is just part of the sort of “treasure hunt” performed during my PhD trying to find a reasonable explanation to the Pioneer Anomaly. Following a trial and error approach, there have been several aspects of the on board systematic (e.g. propulsive system) and of environmental (e.g. ionospheric delay) which have been taken under consideration, modeled, tested, and then disregarded because going not in the right direction. This last assertion is also an admission that my research has been a bit biased by the conviction that the reason underneath the Anomaly had nothing to do with fundamental Physics, but, more prosaically, with human error: an effect which have proved to be safely negligible on almost all of the other spacecrafts, the thermal dissipation force, was firstly ignored also for the Pioneers; this simplification proved to be unjustified.

Conclusions from the results obtained and recommendations for future works are now drawn.

6.1 Conclusions

Orbital solutions for Pioneer 10 and 11 spacecrafts using available radio-metric have been presented. The processing of the data has been carried out in light of the results of a detailed thermal modeling of the spacecraft aiming at evaluating the recoil force due to anisotropic radiation. The thermal model includes main spacecrafts components and has been built using available design documentation and retrieved telemetry data. Monte Carlo simulations allowed for a sensitivity analysis of the solutions, and for a representation of the thermal acceleration along trajectory with a finite number of

Conclusions

parameters. Such a representation is suitable for being incorporated in the process of orbit determination in a consistent manner.

Processing of radio metric data have been performed using the ODP. Single-arc and Multi-arc filtering techniques have been implemented and respective orbit solutions compared. Multi-arc provides a means to compensate for deficiencies in dynamical models when the trajectory arc is very long allowing for a slightly better quality of post-fit residuals. Systematic estimation of velocity increments related to maneuvers have also been included as a necessary step to reach convergence. Validation of ODP usage by the user have been done by comparison of results on the early data set of Pioneer 10 with previously published works.

The results presented shows that the computed thermal recoil acceleration, though not constant in time, is most likely the only responsible for the observed linear drift in the Doppler data, since orbital solutions have been obtained without the needing of any unexplained acceleration in addition to the thermal recoil one. As a further support to this we checked that inclusion of an additional constant acceleration as solve-for parameter does not improve quality of orbital fits and the estimated value is statistically compatible with zero. All these results lead to the same conclusion, namely that no anomalous acceleration is acting on Pioneers spacecrafts as far as all systematic is included during trajectory reconstruction.

6.2 Recommendations

The results presented in this chapter gives as a main indication that the anisotropic thermal radiation is a significant source of acceleration which shall not be neglected for deep space probes orbit determination. One may object that Pioneers seemed to be the only probes requiring this force model: this has been true for many years, but recently Cassini spacecraft provided a remarkable exception (Di Benedetto, M. Iess, L. Roth, 2009). If for Pioneers the magnitude of thermal recoil acceleration was such to highlight its needing only beyond Saturn, Cassini spacecraft characteristics and superior navigation capabilities enlighten the existence of an acceleration of thermal origin in already at Saturn heliocentric distances.

The procedure implemented to account for thermal dissipation force can be adapted for other missions if required: a careful evaluation of such force is highly recommended when accurate navigation is required.

A

Estimation Filters within the ODP

The ODP implements a WLSQ filter which computes a certain vector of parameters as to minimize a cost function. The basics of the mathematical framework behind it are given in this section, adapted from (Moyer, 1971). Specification of estimation formulas to multi arc filtering is taken from (Somenzi, n.d.). First the following quantities shall be defined:

$\hat{\mathbf{z}}$ = column vector of observed observables ($N \times 1$)

\mathbf{z} = vector of computed observables ($N \times 1$)

\mathbf{x} = vector of solve-for parameters ($n \times 1$)

$\tilde{\mathbf{x}}$ = vector of a-priori values of solve-for parameters ($n \times 1$)

\mathbf{y} = vector of consider parameters ($m \times 1$)

$\tilde{\mathbf{y}}$ = vector of a-priori values of consider parameters ($m \times 1$)

The consider parameters affects the observables but are not (or cannot be) estimated. They affects in particular the accuracy of the estimation, that is the covariance matrix of solve-for, but their value is unchanged by the filter, hence $\tilde{\mathbf{y}} = \mathbf{y}$. Uncertainty on a-priori values are defined through the following matrices:

$\tilde{\mathbf{\Gamma}}_{\mathbf{x}}$ = a-priori covariance matrix of $\tilde{\mathbf{x}}$ ($n \times n$);

$\tilde{\mathbf{\Gamma}}_{\mathbf{y}}$ = a-priori covariance matrix of $\tilde{\mathbf{y}}$ ($m \times m$);

$\tilde{\mathbf{\Gamma}}_{\mathbf{xy}}$ = a-priori cross-covariance matrix of $\tilde{\mathbf{x}}$ and $\tilde{\mathbf{y}}$ ($n \times m$).

The observables depend on both \mathbf{x} and \mathbf{y} , which can be stacked into a single parameter vector, \mathbf{q} :

$$\mathbf{q} = \begin{bmatrix} \mathbf{x} \\ \mathbf{y} \end{bmatrix}$$

Appendix A

Whose weighting matrix, \mathbf{W}_q , can be constructed starting from the above covariances as:

$$\mathbf{W}_q = \begin{bmatrix} \tilde{\Gamma}_x & \tilde{\Gamma}_{xy} \\ \tilde{\Gamma}_{xy} & \tilde{\Gamma}_{xy} \end{bmatrix}^{-1} = \begin{bmatrix} \mathbf{W}_x & \mathbf{W}_{xy} \\ \mathbf{W}_{xy} & \mathbf{W}_{xy} \end{bmatrix}$$

Unless sequential batch analysis is performed one can assume a-priori values of solve-for and consider being uncorrelated hence $\tilde{\Gamma}_{xy} = \mathbf{W}_{xy} = \mathbf{0}$.

The column vector of residuals is given by:

$$\mathbf{R} = \begin{bmatrix} \hat{\mathbf{z}} - \mathbf{z} \\ \tilde{\mathbf{x}} - \mathbf{x} \\ \tilde{\mathbf{y}} - \mathbf{y} \end{bmatrix}$$

With these definition, the cost function can be defined as:

$$Q = \mathbf{R}'\mathbf{W}_T\mathbf{R}$$

In the above equation, the apex stands for matrix transpose. \mathbf{W}_T is the weighting matrix for residuals defined as:

$$\mathbf{W}_T = \begin{bmatrix} \mathbf{W} & \mathbf{0} & \mathbf{0} \\ \mathbf{0} & \mathbf{W}_x & \mathbf{0} \\ \mathbf{0} & \mathbf{0} & \mathbf{W}_y \end{bmatrix}$$

\mathbf{W} is a $N \times N$ weighting matrix of observables. With these position, the cost function can be rewritten as:

$$Q = (\hat{\mathbf{z}} - \mathbf{z})'\mathbf{W}(\hat{\mathbf{z}} - \mathbf{z})' + (\tilde{\mathbf{x}} - \mathbf{x})'\mathbf{W}_x(\tilde{\mathbf{x}} - \mathbf{x}) + (\tilde{\mathbf{y}} - \mathbf{y})'\mathbf{W}_y(\tilde{\mathbf{y}} - \mathbf{y}) \quad (10-1)$$

The third addend in the right hand side of eq. (10-1) includes the difference $(\tilde{\mathbf{y}} - \mathbf{y})$ which is always null, but it has is retained since it has to be included while computing the error covariance matrix.

The vector of solve for parameters is then computed as the vector which minimizes Q :

$$\frac{\partial Q}{\partial \mathbf{x}} = \mathbf{0}$$

The above equation can be solved iteratively applying the following, known as *normal equation*:

$$\mathbf{x}^{(k+1)} = \mathbf{x}^{(k)} + (\mathbf{J}^{(k)} + \mathbf{W}_x)^{-1} \left[\mathbf{A}_x^{(k)'} \mathbf{W}(\hat{\mathbf{z}} - \mathbf{z}(\mathbf{x}^{(k)}, \tilde{\mathbf{y}})) + \mathbf{W}_x(\tilde{\mathbf{x}} - \mathbf{x}^{(k)}) \right] \quad (10-2)$$

Where the superscript (k) indicates that the quantity has been computed using the estimated value of \mathbf{x} at the previous step. $(\mathbf{J} + \mathbf{W}_x)$ is called normal matrix. $\mathbf{J} = \mathbf{A}_x' \mathbf{W} \mathbf{A}_x$ is the *information matrix* while \mathbf{A}_x is defined as:

$$\mathbf{A}_x = \frac{\partial \mathbf{z}}{\partial \mathbf{x}} = \begin{bmatrix} \partial z_1 / \partial x_1 & \dots & \partial z_1 / \partial x_n \\ \vdots & \ddots & \vdots \\ \partial z_N / \partial x_1 & \dots & \partial z_N / \partial x_n \end{bmatrix} \quad (10-3)$$

\mathbf{A}_x is the Jacobian matrix which collects the partial derivatives of the observables w.r.t the solve-for parameters. Computation of such matrix is one of the fundamental task of the orbit determination process.

It can be shown that the covariance matrix of the estimated \mathbf{x} vector is given by:

$$\mathbf{\Gamma}_x = (\mathbf{J} + \tilde{\mathbf{\Gamma}}_x^{-1})^{-1} + (\mathbf{J} + \tilde{\mathbf{\Gamma}}_x^{-1})^{-1} \mathbf{L} \mathbf{\Gamma}_y \mathbf{L}' (\mathbf{J} + \tilde{\mathbf{\Gamma}}_x^{-1})^{-1} \quad (10-4)$$

Where $\mathbf{L} = \mathbf{A}'_x \mathbf{W} \mathbf{A}_y$ and $\mathbf{A}_y = \partial \mathbf{z} / \partial \mathbf{y}$.

First term in eq. (10-3) is the covariance in the absence of consider parameters, $\mathbf{\Gamma}_{xNC} = (\mathbf{J} + \tilde{\mathbf{\Gamma}}_x^{-1})^{-1}$, which depends on how the measurement noise is ‘‘mapped’’ through the observational models to the estimated parameters (\mathbf{J}), and on the uncertainty on the a-priori estimates ($\tilde{\mathbf{\Gamma}}_x^{-1}$).

Eq. (10-4) can also be re-written in terms of the so called *sensitivity matrix* defined as: $\mathbf{S}_{xy} = \partial \mathbf{x} / \partial \mathbf{y}$, such that the covariance of the estimate becomes:

$$\mathbf{\Gamma}_x = \mathbf{\Gamma}_{xNC} + \mathbf{\Gamma}_{xy} \tilde{\mathbf{\Gamma}}_y^{-1} \mathbf{\Gamma}_{xy} = \mathbf{S}_{xy} \tilde{\mathbf{\Gamma}}_y \mathbf{S}'_{xy} \quad (10-5)$$

The sensitivity matrix relates the errors in consider parameters to the errors in the estimates of solve-for parameters.

Eq. (10-5) indicates that the effect of consider parameters acts on the accuracy of the estimate with an additive covariance matrix through the cross-covariance matrix $\mathbf{\Gamma}_{xy}$, or, equivalently, through the sensitivity matrix \mathbf{S}_{xy} .

6.3 Square-root implementation

The normal equation described can be numerically inefficient due to the often ill-conditioning of the $(\mathbf{J}^{(k)} + \mathbf{W}_x)$ matrix. A numerical superior algorithm is represented by the so called *square-root form* where the minimization algorithm is reformulated requiring the inversion of a triangular matrix whose condition number is the square root of the condition number of the normal matrix. First, the inverse of a semi-positive definite matrix \mathbf{A} , $\mathbf{A}^{1/2}$, is defined such that $(\mathbf{A}^{1/2})' \mathbf{A}^{1/2} = \mathbf{A}$

Then we rewrite the cost function Q as a function of the square root of \mathbf{W}_T :

$$Q = \|(\mathbf{W}_T^{1/2} \mathbf{R})\|^2 \quad (10-6)$$

This time, rather than minimizing Q , we seek for the minimization of its square root. For this purpose, a differential correction of the parameter vector \mathbf{q} is applied:

$$\delta \mathbf{q} = \begin{bmatrix} \delta \mathbf{x} \\ \mathbf{0} \end{bmatrix}$$

Which leads to a first-order change in the residuals equal to:

$$\mathbf{R}(\mathbf{q} + \delta \mathbf{q}) = \mathbf{R}(\mathbf{q}) + \frac{\partial \mathbf{R}}{\partial \mathbf{q}} \delta \mathbf{q} = \mathbf{R}(\mathbf{q}) - \mathbf{A}_T \delta \mathbf{q} \quad (10-7)$$

Where the matrix \mathbf{A}_T has been defined as:

$$-\mathbf{A}_T = \frac{\partial \mathbf{R}}{\partial \mathbf{q}} = \begin{bmatrix} \partial \mathbf{z} / \partial \mathbf{q} \\ \partial \mathbf{x} / \partial \mathbf{q} \\ \partial \mathbf{y} / \partial \mathbf{q} \end{bmatrix} = \begin{bmatrix} \partial \mathbf{z} / \partial \mathbf{x} & \partial \mathbf{z} / \partial \mathbf{y} \\ \mathbf{I}_n & \mathbf{0} \\ \mathbf{0} & \mathbf{I}_m \end{bmatrix} = \begin{bmatrix} \mathbf{A}_x & \mathbf{A}_y \\ \mathbf{I}_n & \mathbf{0} \\ \mathbf{0} & \mathbf{I}_m \end{bmatrix} \quad (10-8)$$

With this definition, one may write the differentially corrected square root of Q as:

$$Q^{1/2}(\mathbf{q} + \delta \mathbf{q}) = \|\mathbf{W}_T^{1/2} \mathbf{R}(\mathbf{q}) - \mathbf{W}_T^{1/2} \mathbf{A}_T \delta \mathbf{q}\| \quad (10-9)$$

An orthogonal matrix \mathbf{H} shall then be found²¹ for which it holds:

$$\mathbf{H} \mathbf{W}_T^{1/2} \mathbf{A}_T = \begin{bmatrix} \mathbf{R} \\ \mathbf{0} \end{bmatrix} = \begin{bmatrix} \mathbf{R}_x & \mathbf{R}_{xy} \\ \mathbf{0} & \mathbf{R}_y \\ \mathbf{0} & \mathbf{0} \end{bmatrix} \quad (10-10)$$

Where \mathbf{R} , \mathbf{R}_x and \mathbf{R}_y are upper triangular matrices. Since \mathbf{H} is orthogonal we can pre-multiply the right hand side of eq. (10-9) by \mathbf{H} preserving the norm, such that:

$$Q^{1/2} = \|\mathbf{H} \mathbf{W}_T^{1/2} \mathbf{R}(\mathbf{q}) - \mathbf{H} \mathbf{W}_T^{1/2} \mathbf{A}_T \delta \mathbf{q}\| = \left\| \begin{bmatrix} \delta \mathbf{z}_x^* \\ \delta \mathbf{z}_y^* \\ \delta \mathbf{z}_z^* \end{bmatrix} - \begin{bmatrix} \mathbf{R}_x & \mathbf{R}_{xy} \\ \mathbf{0} & \mathbf{R}_y \\ \mathbf{0} & \mathbf{0} \end{bmatrix} \begin{bmatrix} \delta \mathbf{x} \\ \mathbf{0} \end{bmatrix} \right\| = \begin{bmatrix} \delta \mathbf{z}_x^* - \mathbf{R}_x \delta \mathbf{x} \\ \delta \mathbf{z}_y^* \\ \delta \mathbf{z}_z^* \end{bmatrix}$$

Where we denoted the product $\mathbf{H} \mathbf{W}_T^{1/2} \mathbf{R}(\mathbf{q})$ with the vector $[\delta \mathbf{z}_x^* \ \delta \mathbf{z}_y^* \ \delta \mathbf{z}_z^*]$

Minimum for $Q^{1/2}$ is found when $\delta \mathbf{z}_x^* = \mathbf{R}_x \delta \mathbf{x}$, thus, the parameter estimation formula becomes:

$$\delta \mathbf{x} = \mathbf{R}_x^{-1} \delta \mathbf{z}_x^* \quad (10-11)$$

To be iteratively applied similar as for eq. (10-2)

When dealing with multi-arc technique, the above equations can be easily extended by partitioning of \mathbf{q} , \mathbf{R} , \mathbf{W}_T and \mathbf{A}_T . If we consider two arcs, the solve-for parameters are split into global parameters, \mathbf{x} , and local parameter, \mathbf{x}_1 and \mathbf{x}_2 . Then the parameter vector \mathbf{q} is:

²¹ The matrix \mathbf{H} can be computed with a series of Householder orthogonal transformations.

$$\mathbf{q} = \begin{bmatrix} \mathbf{x}_1 \\ \mathbf{x}_2 \\ \mathbf{x} \\ \mathbf{y} \end{bmatrix}$$

The residual vector can be written as:

$$\mathbf{R} = \begin{bmatrix} \hat{\mathbf{z}}_1 - \mathbf{z}_1 \\ \hat{\mathbf{z}}_2 - \mathbf{z}_2 \\ \tilde{\mathbf{x}} - \mathbf{x} \\ \tilde{\mathbf{x}}_1 - \mathbf{x}_1 \\ \tilde{\mathbf{x}}_2 - \mathbf{x}_2 \\ \hat{\mathbf{y}} - \mathbf{y} \end{bmatrix}$$

Where \mathbf{z}_1 and \mathbf{z}_2 are the measurements of the first and second arc respectively.

The weighting matrix is also partitioned in a similar way:

$$\mathbf{W}_T = \text{diag}([\mathbf{W}_1, \mathbf{W}_2, \mathbf{W}_x, \mathbf{W}_{x_1}, \mathbf{W}_{x_2}, \mathbf{W}_y])$$

Where *diag* indicates a block diagonal matrix, and the weighting matrix on the diagonal are defined in an analogous way as for a single arc (correlations between a-priori vectors are again neglected).

The difference to the single arc case is evident from the inspection of the partial matrix \mathbf{A}_T :

$$\mathbf{A}_T = \begin{bmatrix} \frac{\partial \mathbf{z}_1}{\partial \mathbf{q}} \\ \frac{\partial \mathbf{z}_2}{\partial \mathbf{q}} \\ \frac{\partial \mathbf{x}}{\partial \mathbf{q}} \\ \frac{\partial \mathbf{x}_1}{\partial \mathbf{q}} \\ \frac{\partial \mathbf{x}_2}{\partial \mathbf{q}} \\ \frac{\partial \mathbf{x}}{\partial \mathbf{x}} \\ \frac{\partial \mathbf{y}}{\partial \mathbf{q}} \\ \frac{\partial \mathbf{y}}{\partial \mathbf{x}} \\ \frac{\partial \mathbf{y}}{\partial \mathbf{y}} \end{bmatrix} = \begin{bmatrix} \frac{\partial \mathbf{z}_1}{\partial \mathbf{x}_1} & \frac{\partial \mathbf{z}_1}{\partial \mathbf{x}_2} & \frac{\partial \mathbf{z}_1}{\partial \mathbf{x}} & \frac{\partial \mathbf{z}_1}{\partial \mathbf{y}} \\ \frac{\partial \mathbf{z}_2}{\partial \mathbf{x}_1} & \frac{\partial \mathbf{z}_2}{\partial \mathbf{x}_2} & \frac{\partial \mathbf{z}_2}{\partial \mathbf{x}} & \frac{\partial \mathbf{z}_2}{\partial \mathbf{y}} \\ \frac{\partial \mathbf{x}}{\partial \mathbf{x}_1} & \frac{\partial \mathbf{x}}{\partial \mathbf{x}_2} & \frac{\partial \mathbf{x}}{\partial \mathbf{x}} & \frac{\partial \mathbf{x}}{\partial \mathbf{y}} \\ \frac{\partial \mathbf{x}_1}{\partial \mathbf{x}_1} & \frac{\partial \mathbf{x}_1}{\partial \mathbf{x}_2} & \frac{\partial \mathbf{x}_1}{\partial \mathbf{x}} & \frac{\partial \mathbf{x}_1}{\partial \mathbf{y}} \\ \frac{\partial \mathbf{x}_2}{\partial \mathbf{x}_1} & \frac{\partial \mathbf{x}_2}{\partial \mathbf{x}_2} & \frac{\partial \mathbf{x}_2}{\partial \mathbf{x}} & \frac{\partial \mathbf{x}_2}{\partial \mathbf{y}} \\ \frac{\partial \mathbf{x}}{\partial \mathbf{x}_1} & \frac{\partial \mathbf{x}}{\partial \mathbf{x}_2} & \frac{\partial \mathbf{x}}{\partial \mathbf{x}} & \frac{\partial \mathbf{x}}{\partial \mathbf{y}} \\ \frac{\partial \mathbf{y}}{\partial \mathbf{x}_1} & \frac{\partial \mathbf{y}}{\partial \mathbf{x}_2} & \frac{\partial \mathbf{y}}{\partial \mathbf{x}} & \frac{\partial \mathbf{y}}{\partial \mathbf{y}} \end{bmatrix} = \begin{bmatrix} \frac{\partial \mathbf{z}_1}{\partial \mathbf{x}_1} & \mathbf{0} & \frac{\partial \mathbf{z}_1}{\partial \mathbf{x}} & \frac{\partial \mathbf{z}_1}{\partial \mathbf{y}} \\ \mathbf{0} & \frac{\partial \mathbf{z}_2}{\partial \mathbf{x}_2} & \frac{\partial \mathbf{z}_2}{\partial \mathbf{x}} & \frac{\partial \mathbf{z}_2}{\partial \mathbf{y}} \\ \mathbf{I}_{n_1} & \mathbf{0} & \mathbf{0} & \mathbf{0} \\ \mathbf{0} & \mathbf{I}_{n_1} & \mathbf{0} & \mathbf{0} \\ \mathbf{0} & \mathbf{0} & \mathbf{I}_n & \mathbf{0} \\ \mathbf{0} & \mathbf{0} & \mathbf{0} & \mathbf{I}_m \end{bmatrix}$$

which highlights that local parameters are affected only by measurements observed during the arc to which they belong, while the whole set of observations contribute to the estimate of the global parameters.

References

- Anderson, John D, Laing, P. A., Lau, E. L., Liu, A. S., Nieto, M. M., & Turyshev, S. G. (1998). Indication, from Pioneer 10/11, Galileo, and Ulysses Data, of an Apparent Anomalous, Weak, Long-Range Acceleration. *Physical Review Letters*.
- Anderson, J., Laing, P., Lau, E., Liu, A., Nieto, M., & Turyshev, S. (2002). Study of the anomalous acceleration of Pioneer 10 and 11. *Physical Review D*, 65(8), 1-50. doi:10.1103/PhysRevD.65.082004
- Anderson, J.D., Laing, P. A., Lau, E. L., Liu, A. S., Nieto, M. M., & Turyshev, S. G. (2002). Study of the anomalous acceleration of Pioneer 10 and 11. *Physical Review D*, 65(8), 082004. APS. Retrieved from <http://prd.aps.org/abstract/PRD/v65/i8/e082004>
- Bertolami, O., & Páramos, J. (2007). A mission to test the Pioneer anomaly: estimating the main systematic effects. *Arxiv preprint gr-qc/0702149*. Retrieved from <http://arxiv.org/abs/gr-qc/0702149>
- Bertolami, O., Francisco, F., Gil, P. J. S., & Páramos, J. (2008). Thermal analysis of the Pioneer anomaly: A method to estimate radiative momentum transfer. *Arxiv preprint arXiv:0807.0041*, 1-12. Retrieved from <http://arxiv.org/abs/0807.0041>
- Bertolami, O., Francisco, F., Gil, P. J. S., & Páramos, J. (2010). Estimating radiative momentum transfer through a thermal analysis of the Pioneer Anomaly. *Space science reviews*, 151(1), 75–91. Springer. Retrieved from <http://www.springerlink.com/index/w22r6671377nl435.pdf>
- Brownstein, J. R., & Moffat, J. W. (2006). Gravitational solution to the Pioneer 10/11 anomaly. *Classical and Quantum Gravity*, 23(10), 3427-3436. doi:10.1088/0264-9381/23/10/013

References

- Di Benedetto, M. Iess, L. Roth, D. C. (2009). The Non-Gravitational Accelerations of the Cassini Spacecraft. *21st International Symposium on Space Flight Dynamics CNES* (pp. 1-14). Toulouse, France.
- Francisco, F., & Bertolami, O. G., P.J.S. Paramos, J. (2011). Modelling the reflective thermal contribution to the acceleration of the Pioneer spacecraft. *Arxiv: 1103.5222*, 1-11.
- Gilmore, D. G. (2002). *Spacecraft Thermal Control Handbook Volume I: Fundamental Technologies*. (D. G. Gilmore, Ed.) *Integration The Vlsi Journal* (Vol. I). The Aerospace Corporation.
- Jet Propulsion Laboratory Navigation Software Group. (1996). *DPTRAJ-ODP USER'S REFERENCE MANUAL Volume 1. Group* (Vol. 1).
- Klobuchar, J. A. (1975). *A First-Order, Worldwide, Ionospheric, Time-Delay Algorithm. Distribution*.
- L, C., & Rievers, B. (2009). Thermal radiation and the Pioneer anomaly. *Space Technology*.
- Levy, A., Christophe, B., Métris, G., Bériot, P., Courty, J.-M., & Reynaud, S. (2009). ODYSSEY, Orbit Determination Software for the Pioneer Data Analysis. *Space Science Reviews*, 151(1-3), 105-121. doi:10.1007/s11214-009-9596-4
- Markwardt, Craig B. (2002). Independent Confirmation of the Pioneer 10 Anomalous Acceleration. *Ratio*, 29. Retrieved from <http://arxiv.org/abs/gr-qc/0208046>
- Modest, M. F. (2003). *Radiative Heat Transfer*, (Second.). Academic Press.
- Moyer, T. D. (1971). Mathematical formulation of the Double-Precision Orbit Determination Program (DPODP). *Jet Propulsion*. Retrieved from <http://adsabs.harvard.edu/abs/1971mfdo.book.....M>
- Moyer, T. D. (2000). *Formulation for Observed and Computed Values of Deep Space Network Data Types for Navigation*. (J. H. Yuen, Ed.) *Space Communications (Deep Space)*. Pasadena: Deep Space Communications and Navigation Systems Center of Excellence, Jet Propulsion Laboratory.
- Nieto, Michael Martin, Anderson, J. D., & Alamos, L. (n.d.). Using Early Data to Illuminate the Pioneer Anomaly. *Jet Propulsion*.
- Reynaud, S., & Jaekel, M. T. (2008). Tests of general relativity in the solar system. *Arxiv preprint arXiv:0801.3407*, 1-15. Retrieved from <http://arxiv.org/abs/0801.3407>
- Rievers, B., Bremer, S., List, M., Lämmerzahl, C., & Dittus, H. (2010). Thermal dissipation force modeling with preliminary results for Pioneer 10/11. *Acta Astronautica*, 66(3-4), 467-476. doi:10.1016/j.actaastro.2009.06.009

References

- Scheffer, L. (2003). Conventional forces can explain the anomalous acceleration of Pioneer 10. *Physical Review D*, 67(8), 1-11. doi:10.1103/PhysRevD.67.084021
- Somenzi, L. (n.d.). *Multiair analysis and least-squares fit 1. Theory*.
- TRW Systems. (1971). *Pioneer F/G Spacecraft Operational Characteristics PC-202.pdf*.
- Thornton, C. L., & Border, J. S. (n.d.). Radiometric Tracking Techniques for Deep - Space Navigation. *Jet Propulsion*.
- Toth, V., & Turyshev, S. (2009). Thermal recoil force, telemetry, and the Pioneer anomaly. *Physical Review D*, 79(4). doi:10.1103/PhysRevD.79.043011
- Toth, V.T. (2009). Independent analysis of the orbits of Pioneer 10 and 11. *Arxiv preprint arXiv:0901.3466*. Retrieved from <http://arxiv.org/abs/0901.3466>
- Turyshev, Slava G., & Toth, V. T. (2009). The Pioneer Anomaly in the Light of New Data. *Space Science Reviews*, 148(1-4), 149-167. doi:10.1007/s11214-009-9543-4
- Turyshev, S.G., Toth, V. T., Ellis, J., & Markwardt, C. B. (2011). Support for temporally varying behavior of the Pioneer anomaly from the extended Pioneer 10 and 11 Doppler data sets. *Physical Review Letters*, 107(8), 81103. APS. Retrieved from <http://link.aps.org/doi/10.1103/PhysRevLett.107.081103>
- Turyshev, Slava G., & Toth, V. T. (2008). The Pioneer Anomaly. *Arxiv preprint arXiv:0807.1088*, 1-163. Retrieved from <http://arxiv.org/abs/0807.1088>

